ESD-TR-90-087

(2)

Quarterly Technical Report

Solid State Research

1990:2

Lincoln Laboratory

MASSACHUSETTS INSTITUTE OF TECHNOLOGY

LEXINGTON, MASSACHUSETTS

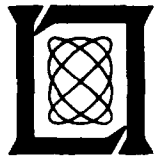

Prepared for the Department of the Air Force under Contract F19628-90-C-0002.

This report is based on studies performed at Lincoln Laboratory, a center for research operated by Massachusetts Institute of Technology. The work was sponsored by the Department of the Air Force under Contract F19628-90-C-0002.

The ESD Public Affairs Office has reviewed this report, and it is releasable to the National Technical Information Service, where it will be available to the general public, including foreign nationals.

This technical report has been reviewed and is approved for publication.

FOR THE COMMANDER

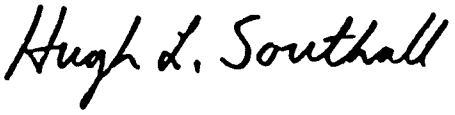

Hugh L. Southall, Lt. Col., USAF
Chief, ESD Lincoln Laboratory Project Office

Non-Lincoln Recipients

PLEASE DO NOT RETURN

Permission is given to destroy this document when it is no longer needed.

MASSACHUSETTS INSTITUTE OF TECHNOLOGY
LINCOLN LABORATORY

SOLID STATE RESEARCH

QUARTERLY TECHNICAL REPORT

1 FEBRUARY — 30 APRIL 1990

ISSUED 14 SEPTEMBER 1990

LEXINGTON MASSACHUSETTS

ABSTRACT

This report covers in detail the research work of the Solid State Division at Lincoln Laboratory for the period 1 February through 30 April 1990. The topics covered are Electrooptical Devices, Quantum Electronics, Materials Research, Submicrometer Technology, Microelectronics, and Analog Device Technology. Funding is provided primarily by the Air Force, with additional support provided by the Army, DARPA, Navy, SDIO, NASA, and DOE.

TABLE OF CONTENTS

LIST OF ILLUSTRATIONS

LIST OF ILLUSTRATIONS (Continued)

LIST OF ILLUSTRATIONS (Continued)

LIST OF ILLUSTRATIONS (Continued)

INTRODUCTION

1. ELECTROOPTICAL DEVICES

Acoustic-wave interactions with integrated-optical modulators on lithium niobate substrates have been found to degrade the modulator performance at frequencies below a few hundred megahertz. Methods developed to suppress these interactions have led to a 90-fold reduction in their effect on the modulator frequency response.

Significant improvements in performance have been achieved for buried GaInP/GaAs double-heterostructure lasers grown by organometallic vapor phase epitaxy and fabricated by mass transport. Threshold currents as low as a 5.5 mA and differential quantum efficiencies as high as 31 percent per facet have been demonstrated.

The polarization-mixing technique has been applied to extend the linear region of interferometric modulators over the frequency range of 3.6 to 5.6 GHz. Intermodulation distortion is reduced by 14 dB at a 3-percent modulation depth, which is equivalent to a 7-dB improvement in power margin for an analog optical link.

2. QUANTUM ELECTRONICS

The beam quality of a Ti:Al_2O_3 master-oscillator/power-amplifier system has been examined by measuring near- and far-field beam profiles. Measurements of the far-field properties of the output beam indicate that it is ~ 1.1 times diffraction limited.

A diode-pumped Nd:YAG laser operating in a single longitudinal and transverse mode has been tuned at an electronics-limited rate of 25 MHz/ns. Tests of voltage-to-frequency conversion gave ~ 1-percent nonlinearity for a 500-MHz frequency chirp in 570 ns.

The theory of single-longitudinal-mode operation of standing-wave laser cavities that was reported previously has been generalized to include the effect of energy diffusion. The resulting analytic expressions have been written in terms of cavity geometry and material parameters.

A thin piece of GaAlAs placed between the Nd:YAG and the output coupler of a microchip laser has been used as a thermal lens to stabilize the laser cavity. The GaAlAs was of the proper composition to transmit light at the output wavelength of the microchip laser, while strongly absorbing the pump light.

A new technique has been developed for mass producing arrays of curved optical surfaces of small numerical aperture. The resulting high-optical-quality surfaces are suitable for curved mirrors in monolithic solid state laser cavities.

Sum-frequency generation of 1.06- and 1.32-μm laser radiation has been carried out using two $LiIO_3$ crystals arranged in series. It was found that, if the crystals are properly oriented, such a tandem arrangement can produce a higher output of frequency-summed radiation than is obtainable with a single crystal.

3. MATERIALS RESEARCH

A technique has been developed for the synthesis and in situ horizontal gradient-freeze growth of InP crystals, without liquid encapsulation, under controlled phosphorus pressures as high as 35 atm. Large-grained ingots were prepared in runs during which the pressure was maintained to ± 0.1 percent over periods of several days.

It has been found that the barrier heights of PtSi-Si Schottky-barrier diodes fabricated on *n*- and *p*-Si substrates are increased and decreased, respectively, by annealing in hydrogen gas, and that subsequent vacuum annealing restores these heights to approximately their as-fabricated values. These results can be attributed to hydrogen passivation of interface detects introduced during contact formation, followed by reactivation of these defects when the hydrogen is removed by vacuum annealing.

4. SUBMICROMETER TECHNOLOGY

The polysilynes, a new class of Si-containing polymers, have been explored as UV photoresists. Features less than 0.4 μm were patterned by combining exposure at 193 nm and development either with organic solvents or in an RF plasma.

Wafer-scale integration techniques have been used to fabricate a high-speed, low-cost mass memory for computer systems, based on 125-mm-diam. wafers with 1-Mbit dynamic random-access memory chips. The fabrication steps included deposition of a planarizing dielectric and two metal levels separated by an additional dielectric.

5. MICROELECTRONICS

Record-high frequencies of operation and power densities have been achieved for resonant-tunneling diodes made from the InAs/AlSb materials system; at 675 GHz the power and power density were ~ 0.5 μW and ~ 25 W cm^{-2}, respectively, and at 360 GHz were 3 μW and 160 W cm^{-2}. The power density measured at 360 GHz is an 80-fold improvement over that for GaAs/AlAs diodes at 370 GHz.

Proton- and neutron-bombarded charge-coupled device (CCD) imagers and related test structures have been measured to determine effects of this irradiation. The minority carrier properties for both *n*- and *p*-type Si were found to be more susceptible to damage with increasing doping level, while measurement of the trap emission time constant suggests that a phosphorus-vacancy complex is the predominant radiation-induced defect limiting the charge transfer efficiency of a CCD.

6. ANALOG DEVICE TECHNOLOGY

Shallow-buried-channel CCDs with a built-in potential gradient in the storage gates have been tested up to 325 MHz with no measurable degradation in the charge transfer efficiency. This is a dramatic improvement in performance relative to conventional designs and is consistent with two-dimensional computer simulations.

An acquisition/preprocessing subsystem has been built for integration with a Nd-laser radar system. The subsystem capabilities include a bandwidth of 200 MHz allowing ~ 1-m range resolution, a range swath of 150 m, and a return rate of up to 80 pulses/s.

REPORTS ON SOLID STATE RESEARCH

1 February through 30 April 1990

PUBLICATIONS

Low-Temperature Laser-Deposition of Tungsten by Silane- and Disilane-Assisted Reactions	J.G. Black S.P. Doran M. Rothschild D.J. Ehrlich	*Appl. Phys. Lett.* **56**, 1072 (1990)
The Extinction Ratio in Optical Two-Guide Coupler $\Delta\beta$ Switches with Asymmetric Detuning	J.P. Donnelly L.A. Molter* G.S. Hopcraft* R.E. Smith* H.A. Haus*	*IEEE J. Quantum Electron.* **26**, 685 (1990)
Pump Source Requirements for End-Pumped Lasers	T.Y. Fan A. Sanchez	*IEEE J. Quantum Electron.* **26**, 311 (1990)
Reduced-Confinement GaAlAs Tapered Waveguide Antenna Grown by Molecular Beam Epitaxy	W.D. Goodhue D.E. Bossi M.C. Finn J.W. Bales R.H. Rediker	*J. Vac. Sci. Technol. B* **8**, 349 (1990)
Growth and Characterization of Ti:$YAlO_3$ for Tunable Solid State Laser Applications	C.P. Khattak* F. Schmid* K.F. Wall R.L. Aggarwal	*Proc. SPIE* **1104**, 95 (1989)
Observation of Maker Fringes and Estimation of $\chi^{(3)}$ Using Picosecond Nondegenerate Four-Wave Mixing in AlGaAs Waveguides	H.Q. Le D.E. Bossi K.B. Nichols W.D. Goodhue	*Appl. Phys. Lett.* **56**, 1008 (1990) DTIC AD-A221419
Wafer Fusion: A Novel Technique for Optoelectronic Device Fabrication and Monolithic Integration	Z.L. Liau D.E. Mull	*Appl. Phys. Lett.* **56**, 737 (1990) DTIC AD-A221147

* Author not at Lincoln Laboratory.

GaInAsP/InP Buried-Heterostructure Surface-Emitting Diode Laser with Monolithic Integrated Bifocal Microlens	Z.L. Liau J.N. Walpole L.J. Missaggia D.E. Mull	*Appl. Phys. Lett.* **56**, 1219 (1990) DTIC AD-A221418
Surface-Energy-Induced Mass Transport Phenomenon in Annealing of Etched Compound Semiconductor Structures: Theoretical Modeling and Experimental Confirmation	Z.L. Liau H.J. Zeiger	*J. Appl. Phys.* **67**, 2434 (1990)
Programmable, Four-Channel, 128-Sample, 40-Ms/s Analog-Ternary Correlator	S.C. Munroe D.R. Arsenault K.E. Thompson A.L. Lattes	*IEEE J. Solid-State Circuits* **25**, 425 (1990)
Stripline Measurements of Surface Resistance: Relation to HTSC Film Properties and Deposition Methods	D.E. Oates A.C. Anderson	*Proc. SPIE* **1187**, 326 (1989)
PtSi Schottky-Barrier Focal Plane Arrays for Multispectral Imaging in Ultraviolet, Visible, and Infrared Spectral Bands	B-Y. Tsaur C.K. Chen J.P. Mattia	*IEEE Electron Device Lett.* **11**, 162 (1990)
Frequency Domain Analysis of Time-Dependent Reflection High-Energy Electron Diffraction Intensity Data	G.W. Turner B.A. Nechay S.J. Eglash	*J. Vac. Sci. Technol. B* **8**, 283 (1990)
Operation of SOI CMOS Devices at Liquid Nitrogen Temperature	K.K. Young B-Y. Tsaur	*IEEE Electron Device Lett.* **11**, 126 (1990) DTIC AD-A221163
Limits Imposed by Spatial Hole Burning on the Single-Mode Operation of Standing-Wave Laser Cavities	J.J. Zayhowski	*Opt. Lett.* **15**, 431 (1990)

ACCEPTED FOR PUBLICATION

Femtosecond Dynamics of the Nonlinear Index Near the Band Edge in AlGaAs Waveguides	K.K. Anderson* M.J. LaGasse* C.A. Wang J.G. Fujimoto* H.A. Haus*	*Appl. Phys. Lett.*

* Author not at Lincoln Laboratory.

Calculation of the Intersubband Absorption Strength in Ellipsoidal Valley Quantum Wells	E.R. Brown S.J. Eglash	*Phys. Rev. B*
Room-Temperature Continuous Operation of GaAs/AlGaAs Lasers Grown on Si by Organometallic Vapor Phase Epitaxy	H.K. Choi C.A. Wang J.C.C. Fan*	*J. Appl. Phys.*
Optical Modulators for Fiber-Optic Sensors	L.M. Johnson	In *Fiber-Optic Sensors: An Introduction for Engineers and Scientists* (Wiley, New York)
Measurements of the Two-Photon Absorption Coefficient in GaAs QuantumWell Lasers	H.Q. Le H.K. Choi C.A. Wang	*Appl. Phys. Lett.*
A New Organometallic Vapor Phase Epitaxy Reactor for Highly Uniform Epitaxy	C.A. Wang	*Lincoln Lab. J.*
Electrical Characterization of Zn^+ and P^+ Co-implanted InP:Fe	J.D. Woodhouse M.C. Gaidis J.P. Donnelly	*Solid-State Electron.*

PRESENTATIONS †

Ti:Al_2O_3 Lasers: From Continuous to Femtosecond Operation	P.A. Schulz	Lincoln Laboratory Technical Seminar Series, Yale University, New Haven, Connecticut, 2 February 1990
High-Frequency Applications of Resonant-Tunneling Devices	T.C.L.G. Sollner E.R. Brown C.D. Parker W.D. Goodhue	Seminar, California Institute of Technology, Pasadena, California, 7 February 1990
CCD Retina and Neural Net Processor	A.M. Chiang	1990 SPIE/SPSE Symposium on Electronic Imaging: Science and Technology, Santa Clara, California, 11-16 February 1990

* Author not at Lincoln Laboratory.

† Titles of presentations are listed for information only. No copies are available for distribution.

Microchip Lasers	J.J. Zayhowski	Seminar, Worcester Polytechnic Institute, Worcester, Massachusetts, 12 February 1990
CVD: Engineering Controls and System Monitoring	S.C. Palmateer S.H. Groves P.A. Greenley*	Seminar, Health and Safety for Microelectronics Laboratories, MIT, Cambridge, Massachusetts, 14 February 1990
A CCD Programmable Signal Processor	A.M. Chiang R.W. Mountain J.H. Reinold J.R. LaFranchise J.A. Gregory G.A. Lincoln	1990 IEEE International Solid-State Circuits Conference, San Francisco, California, 14-16 February 1990
A Full-Fill-Factor CCD Imager with Integrated Signal Processors	W. Yang* A.M. Chiang	
In-Situ Synthesis and Horizontal Gradient-Freeze Growth of InP Crystals	G.W. Iseler	Workshop on Compound Semiconductor Materials and Devices, San Francisco, California, 19 February 1990
Silylation Processes for 193-nm Excimer Laser Lithography	M.A. Hartney R.R. Kunz D.J. Ehrlich D.C. Shaver	SPIE Advances in Microlithography, San Jose, California, 26 February 1990
Homoepitaxial Diamond Films	M.W. Geis	Seminar, Raytheon Research Center, Lexington, Massachusetts, 28 February - 2 March 1990
Superconductive Microwave Circuits	R.W. Ralston	EECS Colloquium Series, MIT, Cambridge, Massachusetts, 5 March 1990

* Author not at Lincoln Laboratory.

Submillimeter-Wave Resonant-Tunneling Oscillators	E.R. Brown	Symposium on Space Terahertz Technology, Ann Arbor, Michigan, 5-7 March 1990
Power Scaling of End-Pumped Lasers by Geometric Multiplexing	T.Y. Fan W.E. DeFeo	Topical Meeting on Advanced Solid-State Lasers, Salt Lake City, Utah, 5-7 March 1990
Diode-Pumped, Self-Starting Additive-Pulse Mode-Locked Nd:YAG and Nd:YLF Lasers	J. Goodberlet* J. Jacobson* J.G. Fujimoto* P.A. Schulz T.Y. Fan	
Self-Starting Dynamics of a Passively Mode-Locked Ti:Al_2O_3 Laser	J. Goodberlet* J. Wang* J.G. Fujimoto* P.A. Schulz	
Laser Pumping of Solid-State Amplifiers Using Random Binary Phase Plates	P. Lacovara K.F. Wall R.L. Aggarwal M.W. Geis K. Krohn	
A Ti:Al_2O_3 Master-Oscillator–Power-Amplifier System	K.F. Wall R.L. Aggarwal P.A. Schulz P. Lacovara V. Daneu A. Walther	
Thermal Waveguiding in Microchip Lasers	J.J. Zayhowski	
Two-Dimensional Surface-Emitting Diode Laser Arrays	R.C. Williamson	Lincoln Laboratory Technical Seminar Series, University of Illinois, Champaign-Urbana, Illinois, 7 March 1990

* Author not at Lincoln Laboratory.

$Ti:Al_2O_3$ Lasers: From Continuous to Femtosecond Operation	P.A. Schulz	Lincoln Laboratory Technical Seminar Series, University of Colorado, Boulder, Colorado, 8 March 1990
Integrated Optics	L.M. Johnson	Seminar, IEEE Waterloo Chapter, Waterloo, Ontario, 14 March 1990
Diamond Devices	M.W. Geis	Meeting of the American Physical Society, Anaheim, California, 15 March 1990
Observation of Optically Pumped Intersubband Emission from Quantum Wells	J.W. Bales A.K. McIntosh T.C.L.G. Sollner W.D. Goodhue E.R. Brown	SPIE Conference on Frontiers of High Speed Electronics and Device Scaling, San Diego, California, 17-21 March 1990
High-Speed and High-Power-Density Oscillations in Resonant Tunneling Diodes Made from Pseudomorphic $In_{0.53}Ga_{0.47}As$/AlAs System	E.R. Brown C.D. Parker T.C.L.G. Sollner A.R. Calawa M.J. Manfra C.L. Chen S.W. Pang K.M. Molvar	
Electronic Applications of High-T_c Superconducting Films	R.S. Withers	SPIE High-T_c Superconductivity Short Course, San Diego, California, 17-21 March 1990
Plasma-Deposited Amorphous Carbon Planarizing Layers	M.W. Horn	Seminar, Digital Equipment Corporation, Hudson, Massachusetts, 20 March 1990
High-Performance Optical Analog Links Using External Modulators	G.E. Betts L.M. Johnson C.H. Cox III	DoD Fiber Optics Conference '90, McLean, Virginia, 20-23 March 1990

High-Power Surface-Emitting Diode Lasers	J.N. Walpole	DoD Fiber Optics Conference '90, McLean, Virginia, 20-23 March 1990
Suppression of Acoustic Effects in Lithium Niobate Integrated Optical Modulators	G.E. Betts K.G. Ray L.M. Johnson	Topical Meeting on Integrated Photonics Research, Hilton Head, South Carolina, 26-28 March 1990
Impedance and Loss Calculations for Thick Coplanar Structures for Optical Modulators	A. Gopinath* J.P. Donnelly	
High-Sensitivity 1.3-GHz Bandpass Interferometric Modulator	L.M. Johnson H.V. Roussell	
OMVPE Growth of Low-Threshold, High-Efficiency GaAs/AlGaAs and Strained-Layer InGaAs/AlGaAs Diode Lasers	C.A. Wang H.K. Choi	
Progress in Diode-Pumped Solid-State Lasers	T.Y. Fan	Seminar, Kansas State University, Manhattan, Kansas, 28 March 1990
Measurement of the Surface Resistance of Thin Films Using Stripline Resonators	D.E. Oates A.C. Anderson P.M. Mankiewich*	Symposium on High Temperature Superconductors in High Frequency Fields, Williamsburg, Virginia, 28-30 March 1990
Third-Order Optical Nonlinearities in Semiconductor Heterostructures	H.Q. Le	Seminar, Philips Laboratories, Briarcliff Manor, New York, 29 March 1990
Plasma-Deposited Amorphous Carbon Planarizing Layers	M.W. Horn	Seminar, Motorola, Mesa, Arizona, 3 April 1990
Superconductive Microwave Devices and Circuits	R.S. Withers	Seminar, Raytheon Research Center, Lexington, Massachusetts, 4 April 1990

* Author not at Lincoln Laboratory.

Compact, Single-Frequency, Electro-optically Tuned Nd:YAG Laser	S.R. Henion P.A. Schulz	Meeting of the New England Section of the American Physical Society, Lowell, Massachusetts, 6-7 April 1990
Semiconductor Lasers with Monolithic Micro-optics for Large-Scale Integration	Z.L. Liau	Seminar, University of California, Irvine, 12 April 1990
Dry Resists for Deep-UV Submicrometer Lithography	M.W. Horn	Seminar, Pennsylvania State University, University Park, Pennsylvania, 16 April 1990
Multichip Interconnect Technique for Optoelectronic Components	C.L. Chen L.J. Mahoney D.Z. Tsang K.M. Molvar S.P. Doran V. Diadiuk	SPIE Conference on Optical and Digital GaAs Technologies for Signal Processing Applications, Orlando, Florida, 16-18 April 1990
High-Speed Optical Interconnections Between Digital Circuits	D.Z. Tsang	
Quantum Well Photodetectors	S.J. Eglash	1990 Spring Workshop on Quantum Well Semiconductor Devices, Waltham, Massachusetts, 17 April 1990
Horizontal Gradient-Freeze Growth of InP Crystals Under Controlled Pressure	G.W. Iseler H.R. Clark, Jr.	Second International Conference on InP and Related Materials, Denver, Colorado, 23-25 April 1990
Growth and Fabrication of $Ga_{0.51}In_{0.49}P$/GaAs Buried-Heterostructure Lasers	S.C. Palmateer S.H. Groves Z.L. Liau J.N. Walpole	
The Lincoln Laboratory 193-nm Lithography Program	D.C. Shaver	Topical Research Conference on Lithography, Berkeley, California, 26 April 1990

ORGANIZATION

SOLID STATE DIVISION

A.L. McWhorter, *Head*
I. Melngailis, *Associate Head*
E. Stern, *Associate Head*
J.F. Goodwin, *Assistant*

D.J. Ehrlich, *Senior Staff*
N.L. DeMeo, Jr., *Associate Staff*
J.W. Caunt, *Assistant Staff*
K.J. Challberg, *Administrative Staff*

SUBMICROMETER TECHNOLOGY

D.C. Shaver, *Leader*
M. Rothschild, *Assistant Leader*

Astolfi, D.K.
Craig, D.M.
Dennis, C.L.
Doran, S.P.
Efremow, N.N., Jr.
Forte, A.R.
Gajar, S.A.*
Geis, M.W.
Goodman, R.B.
Hartney, M.A.
Horn, M.W.
Kunz, R.R.
Lyszczarz, T.M.
Maki, P.A.
Melngailis, J.†
Sedlacek, J.H.C.
Uttaro, R.S.

QUANTUM ELECTRONICS

A. Mooradian, *Leader*
P.L. Kelley, *Associate Leader*
A. Sanchez-Rubio, *Assistant Leader*

Aggarwal, R.L.
Barch, W.E.
Belanger, L.J.
Cook, C.C.
Daneu, V.
DeFeo, W.E.
DiCecca, S.
Dill, C.D., III
Fan, T.Y.
Hancock, R.C.
Henion, S.R.
Hotaling, T.C.
Hsu, L.*
Jeys, T.H.
Korn, J.A.
Lacovara, P.
Le, H.Q.
Menyuk, N.†
Nabors, C.D.
Ochoa, J.R.
Schulz, P.A.
Seemungal, W.A.
Sullivan, D.J.
Wall, K.F.
Zayhowski, J.J.

ELECTRONIC MATERIALS

A.J. Strauss, *Leader*
B-Y. Tsaur, *Associate Leader*
H.J. Zeiger, *Senior Staff*

Anderson, C.H., Jr.
Button, M.J.
Chen, C.K.
Choi, H.K.
Clark, H.R., Jr.
Connors, M.K.
Delaney, E.J.
Eglash, S.J.
Fahey, R.E.
Finn, M.C.
Iseler, G.W.
Kolesar, D.F.
Krohn, L., Jr.
Mastromattei, E.L.
Mattia, J.P.*
McGilvary, W.L.
Nechay, B.A.
Nitishin, P.M.
Pantano, J.V.
Tracy, D.M.
Turner, G.W.
Wang, C.A.

* Research Assistant
† Part Time

APPLIED PHYSICS

R.C. Williamson, *Leader*
D.L. Spears, *Assistant Leader*
R.H. Rediker, *Senior Staff*

Aull, B.F.
Bailey, R.J.
Barwick, D.S.*
Betts, G.E.
Corcoran, C.J.*
Cox, C.H., III
Diadiuk, V.
Donnelly, J.P.
Ferrante, G.A.
Groves, S.H.
Harman, T.C.
Hovey, D.L.
Johnson, L.M.
Liau, Z.L.
Lind, T.A.
Missaggia, L.J.
Mull, D.E.
O'Donnell, F.J.
Palmacci, S.T.
Palmateer, S.C.
Pheiffer, B.K.*
Rauschenbach, K.
Reeder, R.E.
Roussell, H.V.
Shiple, S.D.*
Tsang, D.Z.
Walpole, J.N.
Woodhouse, J.D.
Yee, A.C.

ANALOG DEVICE TECHNOLOGY

R.W. Ralston, *Leader*
R.S. Withers, *Associate Leader*
T.C.L.G. Sollner, *Assistant Leader*
R.M. Lerner, *Senior Staff*†

Anderson, A.C.
Arsenault, D.R.
Bhushan, M.
Boisvert, R.R.
Brogan, W.T.
Denneno, A.P.
Fitch, G.L.
Green, J.B.
Hamm, J.M.
Holtham, J.H.
Lattes, A.L.
Lichtenwalner, D.J.*
Lyons, W.G.
Macedo, E.M., Jr.
Minnick, R.G.
Munroe, S.C.
Oates, D.E.
Sage, J.P.
Seaver, M.M.
Shih, B.S.*
Slattery, R.L.
Westerheim, A.C.*
Whitley, D.B.
Yu-Jahnes, L-S.*

MICROELECTRONICS

R.A. Murphy, *Leader*
E.D. Savoye, *Associate Leader*
B.B. Kosicki, *Assistant Leader*
R.W. Chick, *Senior Staff*

Actis, R.
Bales, J.W.*
Bergeron, N.J.
Bozler, C.O.
Brown, E.R.
Burke, B.E.
Calawa, A.R.
Chen, C.L.
Chiang, A.M.
Chuang, M.L.*
Clifton, B.J.
Cooper, M.J.
Crenshaw, D.L.*
Daniels, P.J.
Doherty, C.L., Jr.
Dolat, V.S.
Donahue, T.C.
Durant, G.L.
Felton, B.J.
Gladden, D.B.‡
Goodhue, W.D.
Gray, R.V.
Gregory, J.A.
Hollis, M.A.
Huang, C.M.
Hurley, E.T.
Johnson, B.W.
Johnson, K.F.
LaFranchise, J.R.
Lincoln, G.A., Jr.
Mahoney, L.J.
Manfra, M.J.
Mathews, R.H.
McGonagle, W.H.
McIntosh, K.A.
McMorran, R.A.
Mountain, R.W.
Nichols, K.B.
Parker, C.D.
Percival, K.A.
Pichler, H.H.
Rabe, S.
Rathman, D.D.
Reich, R.K.
Reinold, J.H., Jr.
Smith, F.W.
Vera, A.
Young, D.J.

* Research Assistant
† Part Time
‡ Staff Associate

1. ELECTROOPTICAL DEVICES

1.1 SUPPRESSION OF ACOUSTIC EFFECTS IN $LiNbO_3$ INTEGRATED-OPTICAL MODULATORS

Acoustic effects can degrade the performance of lithium niobate integrated-optical modulators at frequencies below a few hundred megahertz. Various acoustic problems have been reported in traveling-wave modulators [1] and in lumped-element modulators using both baseband [2] and resonant [3] drive circuits. The most serious effect is the appearance of ripples in the frequency response due to acoustic resonances, as seen in Figure 1-1(a). These are typically very sharp (as little as 100 kHz wide) and are polarization dependent. Acoustic interactions also lead to frequency-dependent changes in the modulator electrode impedance, causing problems primarily in resonant-matched devices. Finally, acoustic waves can create crosstalk between modulators on the same substrate. All of these effects can be drastically reduced by modifying the modulator and substrate to damp out acoustic resonances.

Our experimental measurements are primarily from Mach-Zehnder intensity modulators fabricated on *X*-cut $LiNbO_3$. These used lumped-element electrodes of 5- to 55-mm length, having 6-μm-wide gaps separated by 26 to 130 μm. We measured the frequency response, the modulator impedance, and on some devices the electrical impulse response. All of the specific results quoted here are from *X*-cut devices. We have performed several of the same measurements on devices built on *Z*-cut optical waveguide substrates and on *Y*-cut and 128°-cut surface acoustic wave (SAW) substrates, and our results on these crystal cuts are similar to those reported here for *X*-cut substrates.

The frequency response measures the square of the optical modulation depth as a function of frequency for a constant RF input power. We have seen acoustic effects over the entire 3-MHz to 1-GHz frequency range used in our tests, but the most severe effects are at lower frequencies, under about 200 MHz. For the *Z*-polarized (TE) optical mode the worst ripples were about 1.5 dB peak to peak, and for the *X*-polarized (TM) mode the ripples were up to 9 dB. These measurements were made with a 50-Ω termination in parallel with the modulator. When a resonant impedance match [3] was used, the ripples became much more severe.

The modulator input impedance was measured by connecting the electrodes directly to a network analyzer and looking at the reflected RF power. This measurement showed two effects: rapid fluctuations in impedance as a function of frequency due to acoustic resonances, and an increase in the modulator equivalent series resistance over a broad frequency range due to launching of acoustic wave power. The highest equivalent series resistance occurs in the frequency range where the electrode gap spacing is about one-half wavelength for the *Z*-propagating shear wave (on the *X*-cut modulator). The equivalent series resistance decreases with increasing electrode length. These observations roughly agree with analyses of acoustic transducers performed in connection with SAW devices [4].

We made electrical time-domain (impulse) measurements on a few devices to help identify where acoustic reflections occurred. In this measurement, we applied a 10-ns electrical pulse to the modulator electrodes and then looked for return pulses caused by reflected acoustic pulses inducing voltage pulses in the electrodes. The strongest reflection occurred with a time delay corresponding to reflection of the

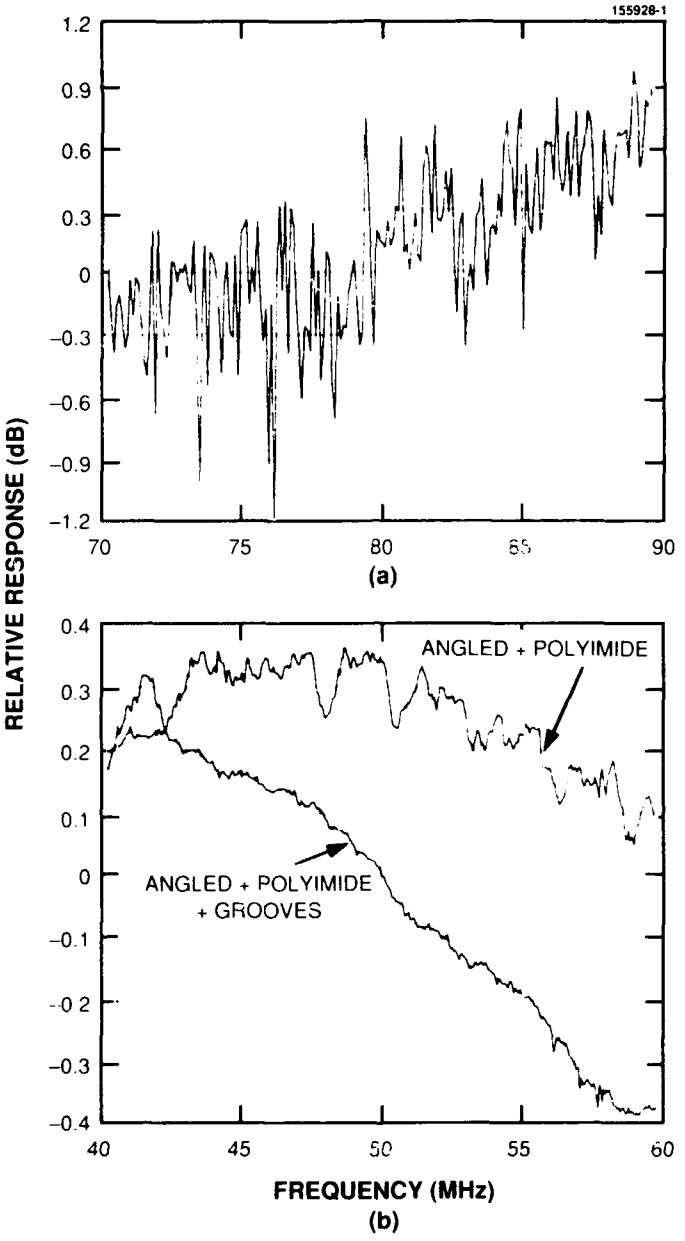

Figure 1-1. Frequency response of modulators with and without acoustic mode suppression, using the Z-polarized (TE) optical mode. (a) Modulator with no acoustic suppression. (b) Modulators with the back side angled and both sides coated with polyimide, with and without grooves cut in the back.

bulk shear wave from the bottom of the substrate; the next strongest reflection corresponded to reflection of the bulk longitudinal wave from the bottom of the substrate. These measurements strongly suggest that the primary resonances are bulk-wave resonances involving reflections from the bottom of the substrate.

Based on the above observations, we have successfully applied various techniques in an attempt to suppress acoustic effects. These modifications are illustrated in Figure 1-2, which shows a cross-sectional view of an integrated-optical interferometric modulator. Grinding the bottom side at an angle [3],[5] and cutting grooves in it act to scatter the acoustic power impinging on the bottom side, which spoils the acoustic reflection. The acoustic wavelength is fairly long at low frequencies, 70 μm at 50 MHz, for example, so variations in the surface need to be fairly large to effectively scatter the acoustic waves. Polyimide is a good acoustic absorber on $LiNbO_3$. On the top surface it damps out SAWs, and on both surfaces it helps to absorb bulk waves. Changing the electrode gap separation changes the frequency at which the acoustic effects are the strongest, and in some applications this may be used to move acoustic problems away from the frequency of interest. For example, a device with a 130-μm separation had small resonances and low equivalent series resistance above about 45 MHz (as opposed to about 100 MHz for a device with a 56-μm separation). These techniques need not all be used together; each one gives some improvement.

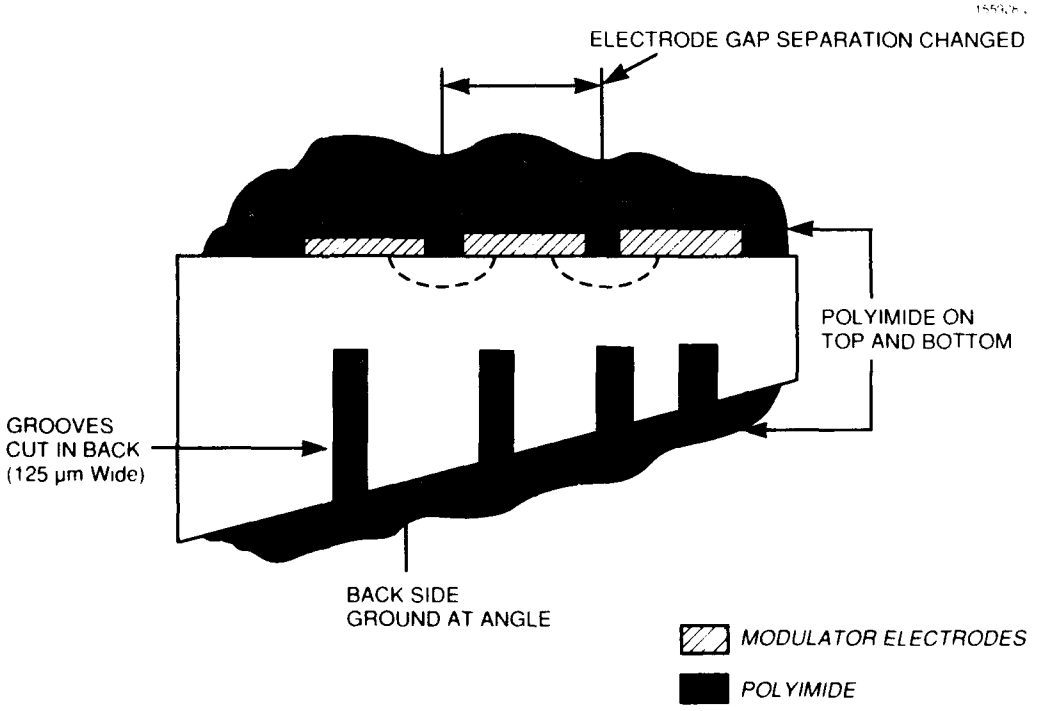

Figure 1-2. Cross-sectional view of an integrated-optical interferometric modulator on X-cut $LiNbO_3$, showing the modifications made to suppress acoustic effects.

Figure 1-1(b) shows the results of acoustic suppression. Suppression both reduces the magnitude of the ripple and broadens the resonances. Grinding the back side at an angle and coating both sides with polyimide reduces the ripple from 1.5 dB peak to peak to about 0.13 dB. Cutting grooves in the back side in addition to the angling and the polyimide coating further reduces the ripple to about 0.02 dB. The degree of suppression needed depends upon the particular application for the modulator.

G.E. Betts L.M. Johnson
K.G. Ray R.C. Williamson

1.2 IMPROVED MASS-TRANSPORTED GaInP/GaAs LASERS

Recently, buried-heterostructure (BH) lasers were fabricated in GaInP/GaAs double-heterostructure (DH) wafers using mass transport. This work [6],[7] was the first demonstration of mass-transport fabrication techniques applied to lasers emitting in the 800- to 900-nm wavelength range ($\lambda \approx 890$ nm was observed for the GaAs active regions). It was also the first demonstration of organometallic vapor phase epitaxy (OMVPE) of DH lasers in this material system, where the wide-bandgap layers consisted of $Ga_{0.51}In_{0.49}P$, rather than the conventional AlGaAs alloys. Significant advantages should be obtained using OMVPE instead of hydride vapor phase [8] and liquid phase [9] epitaxy, which have previously been used to grow GaInP/GaAs lasers.

Here, we report further improvements in the performance of these BH lasers. Devices with an active-buried-stripe width of 1.5 to 2.0 μm and a cavity length of 150 μm have yielded threshold currents as low as 5.5 mA, as shown in Figure 1-3, where pulsed light output from a device is plotted versus current. The linearity of the characteristics in this figure indicate that leakage current is small. An

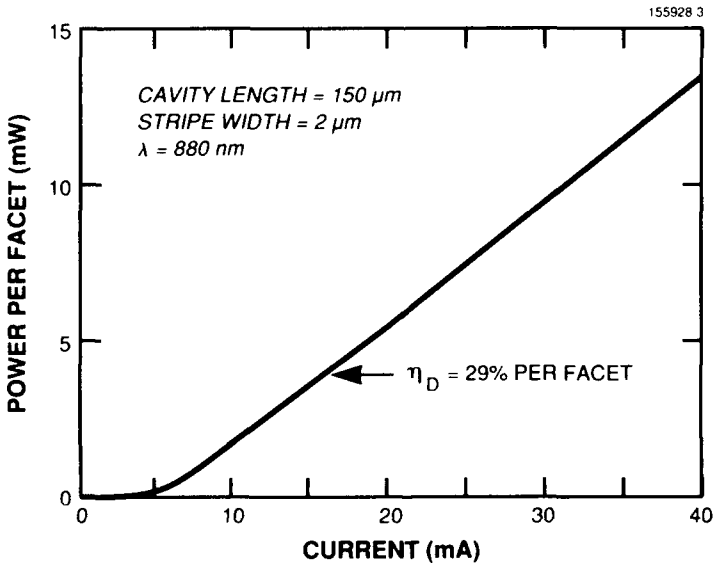

Figure 1-3. Pulsed output power of mass-transported GaAs laser as a function of diode current.

external differential efficiency η_D of up to 31 percent per facet was observed for the 150-μm cavity length. For a 350-μm-long device, an η_D of 24.5 percent per facet and a threshold current of 9 mA were measured, which correspond to a loss coefficient of about 35 cm^{-1} and a threshold current density of about 1.3 to 1.7 kA/cm^2 for 1.5- to 2.0-μm-wide BH lasers. For comparison, in broad-stripe (200 μm wide) lasers, the threshold current density is 1.1 kA/cm^2. Lasers with 9-mA pulsed threshold current showed no appreciable increase in threshold under CW operation. The emission wavelength of the improved BH lasers was about 880 nm.

The improvements are due to better OMVPE growth of the heterointerfaces and to refinements in the mass-transport fabrication technique. Figure 1-4 shows a cross section of the BH structure obtained after mass transport. In earlier work [10], in order to avoid complicating surface chemistry and transport, the GaAs contact layer was fully confined by GaInP during the heat treatment to bury the active region. Here, it has been determined that the oxide etch mask is sufficient for this purpose. As a result, one of the two heat treatment steps used in the earlier process is eliminated, and the growth and subsequent removal of a protecting GaInP layer are not needed.

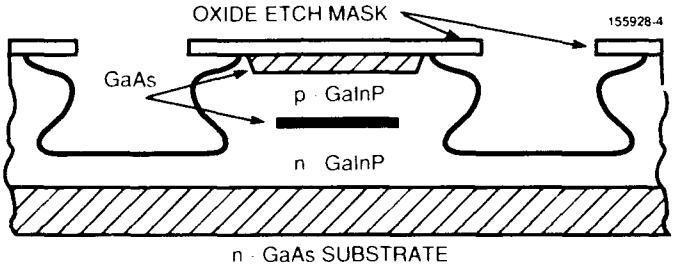

(a)

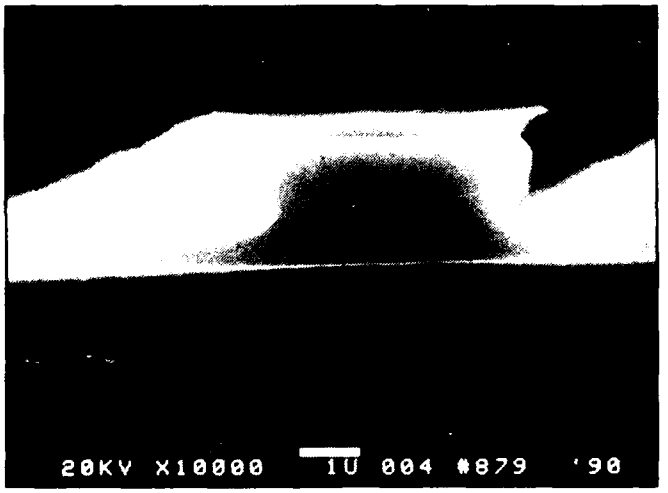

(b)

Figure 1-4. Buried-heterostructure laser. (a) Schematic cross section. (b) Scanning electron micrograph of a cross section of a cleaved device.

In continuing to develop these lasers, we are employing quaternary GaInAsP alloys for wider bandgaps and are working to grow quantum-well and strained-layer devices. These advances in combination with mass-transport technology open many exciting possibilities for lasers, including nonabsorbing mirrors, integrated lenses, and surface-emitting devices. Also, mass-transported BH lasers have a mesa geometry that minimizes parallel-junction capacitance and makes very high speed modulation possible. Indeed, 1.3-μm-wavelength lasers with similar mass-transported mesa structures have shown modulation bandwidths up to 16 GHz [11]. Work is under way to demonstrate this capability with the present devices, and preliminary measurements indicate a –3-dB frequency of at least 8 to 9 GHz.

S.H. Groves
Z.L. Liau
L.J. Missaggia
S.C. Palmateer
D.Z. Tsang
J.N. Walpole

1.3 LINEARIZATION OF AN INTERFEROMETRIC MODULATOR AT MICROWAVE FREQUENCIES BY POLARIZATION MIXING

High-performance analog optical links have been demonstrated using external integrated-optical intensity modulators [12]. A critical parameter affecting the dynamic range and/or power margin of these links is the modulator linearity. In a previous report [13],[14], a polarization-mixing linearization technique for reducing intermodulation (IM) distortion in interferometric modulators was described. Since the technique does not require high-speed electronics, it appears particularly advantageous for microwave-frequency analog optical links. Here, we describe the linearization of an interferometric modulator by polarization mixing over the suboctave frequency range of 3.6 to 5.6 GHz. At a modulation depth of 3 percent, two-tone IM distortion is reduced by ~ 14 dB as compared to conventional operation.

The polarization-mixing technique for reducing modulator nonlinearities is applicable to interferometric modulators supporting two polarization modes with differing electrooptic sensitivities. Normally, these modulators are operated with all of the optical power coupled into the polarization mode with the highest sensitivity. The polarization-mixing technique, on the other hand, involves using both polarization modes simultaneously. By adjusting the phase biases such that the transfer functions of the two modes have slopes of opposite sign and by adjusting the relative optical power in each mode, the modulator nonlinearities can be substantially reduced. Under ideal conditions, both the second-order and cubic nonlinearities can be eliminated. Since most of the optical power is coupled into the less sensitive polarization mode, there is an overall reduction in modulator sensitivity, but for a fixed modulation index there can be a significant reduction in distortion levels.

A link in which the linear region is extended by the polarization-mixing technique can be configured as shown in Figure 1-5. The transmitter contains a CW laser, an interferometric external modulator, and a polarizer to maintain the proper modulator input polarization. It is important to note that polarization control of the modulated signal is not required. Therefore, conventional single-mode optical fiber can be used, and polarization-preserving fiber is not necessary.

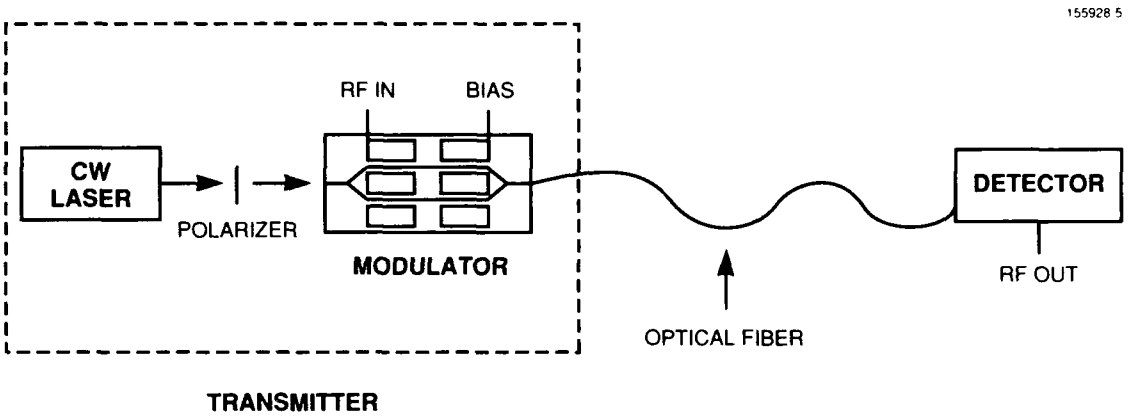

Figure 1-5. Schematic illustration of an externally modulated analog optical link in which the linear region is extended by the polarization-mixing technique. The transmitter consists of a CW laser, an optical polarizer and an interferometric modulator. The modulated optical signal can be transmitted on conventional single-mode optical fiber.

The objective of the present experiment was to minimize two-tone IM distortion resulting from the cubic nonlinearity in the modulator. This is often the dominant distortion component for suboctave applications. A traveling-wave modulator fabricated in *X*-cut $LiNbO_3$ utilizing the r_{33} (TE) and r_{13} (TM) electrooptic coefficients was employed. Over the frequency range of 3.6 to 5.6 GHz, the effective V_π values (from a 50-Ω source) were 14 and 43 V for the TE and TM modes, respectively. The modulator response was not optimized for this frequency range. A dc voltage was applied to separate bias electrodes to adjust the relative TE and TM phase bias, and a polarizer was placed between the diode-pumped Nd:YAG laser source and the modulator to adjust the relative TE and TM optical power. The output was measured with a high-speed photodetector and spectrum analyzer.

The modulator response was first measured for conventional single-polarization TE operation. Two tones spaced 5 MHz apart with a power level of –5 dBm per tone were applied at a series of frequencies from 3.6 to 5.6 GHz. This resulted in a modulation depth of 3 percent at the fundamental frequencies and IM distortion of ~ –80 dBc, as plotted in Figure 1-6. For two-polarization operation, the polarizer was adjusted to couple 95 and 5 percent of the light into the TM and TE modes, respectively, and the modulator bias voltage was then adjusted to minimize the IM distortion. The electrical drive power was increased to 5 dBm per tone to maintain the 3-percent modulation depth at the fundamental frequencies. As can be seen in Figure 1-6, the relative IM distortion decreased by ~ 14 dB across the band. Both the polarizer setting and the bias voltage were left unchanged during the series of measurements. This reduction in IM distortion is equivalent to a 7-dB increase in the link power margin.

L.M. Johnson
H.V. Roussell

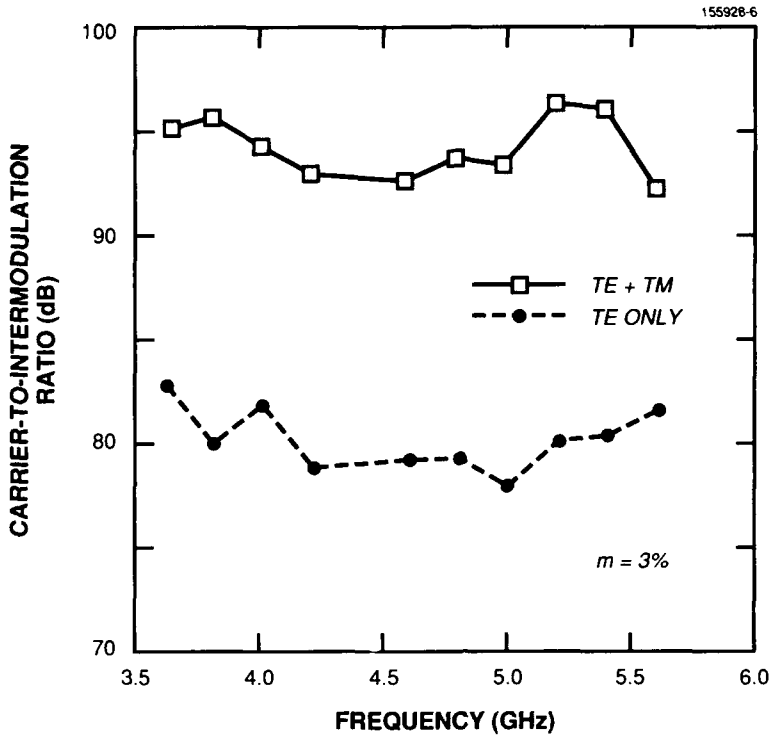

Figure 1-6. Carrier-to-intermodulation ratio as a function of modulation frequency for an interferometric modulator. The dashed line indicates single-polarization operation (TE), and the solid line shows dual-polarization operation (TE and TM). For both cases the modulation depth m is 3 percent.

REFERENCES

1. R.L. Jungerman and C.A. Flory, *Appl. Phys. Lett.* **53**, 1477 (1988).
2. J.L. Nightingale, R.A. Becker, P.C. Willis, and J.S. Vrhel, *Proc. SPIE* **835**, 108 (1987).
3. G.E. Betts, L.M. Johnson, and C.H. Cox III, *J. Lightwave Technol.* **7**, 2078 (1989).
4. W.R. Smith, H.M. Gerard, J.H. Collins, T.M. Reeder, and H.J. Shaw, *IEEE Trans. Microwave Theory Tech.* **MTT-17**, 856 (1969).
5. A. Nishiwaki, S. Hattori, Y. Kato, Y. Hiraiwa, T. Hiramatu, H. Hoshikawa, and M. Katayama, *Opt. Laser Technol.* **11**, 37 (1979).
6. S.H. Groves, Z.L. Liau, S.C. Palmateer, and J.N. Walpole, *Appl. Phys. Lett.* **56**, 312 (1990).
7. Solid State Research Report, Lincoln Laboratory, MIT (1989:3), p. 5.
8. C.J. Nuese, G.H. Olsen, and M. Ettenberg, *Appl. Phys. Lett.* **29**, 54 (1976).

9. Zh.I. Alferov, N. Yu Antonishkis, I.N. Arsent'ev, D.Z. Garbuzuv, V.I. Kolyskin, T.A. Nalet, N.A. Strugov, and A.V. Tikunov, *Fiz. Tekh. Poluprovodn.* **22**, 1031 (1988) [*Sov. Phys. Semicond.* **22**, 650 (1988)].

10. Solid State Research Report, Lincoln Laboratory, MIT (1989:2), p. 11.

11. D.Z. Tsang and Z.L. Liau, *J. Lightwave Technol.* **LT-5**, 300 (1987).

12. G.E. Betts, L.M. Johnson, C.H. Cox III, and S.D. Lowney, *IEEE Photon. Technol. Lett.* **1**, 404 (1989).

13. Solid State Research Report, Lincoln Laboratory, MIT (1988:2), p. 2. DTIC AD-A204718.

14. L.M. Johnson and H.V. Roussell, *Opt. Lett.* **13**, 928 (1988).

2. QUANTUM ELECTRONICS

2.1 BEAM QUALITY OF A TI:Al_2O_3 MASTER-OSCILLATOR/POWER-AMPLIFIER SYSTEM

We have previously reported [1] on the operation of a longitudinally pumped, multistage Ti:Al_2O_3 master-oscillator/power-amplifier (MOPA) system designed to produce pulsed (10 Hz), tunable radiation from 750 to 850 nm. Single-frequency output of 100-ns, 0.38-J pulses at 800 nm was obtained. In this report, we further describe the Ti:Al_2O_3 MOPA system in terms of its near- and far-field beam characteristics.

The system consists of a CW, single-frequency, TEM_{00} Ti:Al_2O_3 ring laser as a master oscillator and four Ti:Al_2O_3 amplifier stages. Each amplifier stage consists of a single Brewster-cut Ti:Al_2O_3 crystal pumped by a pulsed (10 Hz), frequency-doubled Nd:YAG laser in a nearly collinear geometry. Several of the Ti:Al_2O_3 amplifier stages are multipassed to increase the signal gain; the overall signal gain of the system is $\sim 2 \times 10^7$. Significant aberrations of the signal beam can occur as a result of the large number of passes through gain regions (nine), reflections from mirrors (twenty-eight), and transmissions through surfaces (ninety-three). In order to quantify these effects, the near- and far-field properties of the output beam were investigated.

A commercially available beam profiler was used to obtain near-field profiles (~ 2 m from the output of the final amplifier stage). A density plot of a typical near-field profile from the output of the Ti:Al_2O_3 MOPA system at $\lambda = 800$ nm is shown in Figure 2-1(a), where the darker shading represents higher intensity. Profiles through the centroid of the data in the horizontal and vertical directions are shown in Figures 2-1(b) and (c), respectively, where the data are indicated by the solid circles, and the solid lines are Gaussian fits to the data. The fits to the data indicate that the beam can be characterized as elliptically Gaussian in nature. The energy per pulse was ~ 340 mJ.

The beam profile at the focus of a 1-m lens was measured to investigate the far-field properties of the output beam. The density plot of the far-field profile is shown in Figure 2-2(a), and profiles through the centroid of the data are shown in Figures 2-2(b) and (c). Again, the beam can be characterized as elliptically Gaussian in nature, but with the major and minor axes of the ellipse reversed compared with Figure 2-1. A problem with the above measurement is that it is possible that most of the beam energy could be contained in a broad, low-intensity pedestal, which would not be registered by the detector used to obtain the beam profiles because of the detector's limited dynamic range (~ 40:1). This would lead to an overly optimistic estimate of the far-field beam quality.

A second method used to examine the far-field properties of the output beam does not suffer from dynamic range problems. The "energy in a bucket" was estimated by measuring the transmission of the focused output through circular apertures of various sizes. The signal beam was sampled by taking a reflection from a wedge and was focused with a 1-m lens. A pinhole was positioned at the focus of the lens and was centered by maximizing the transmission. If we assume that the beam waist at the focus of

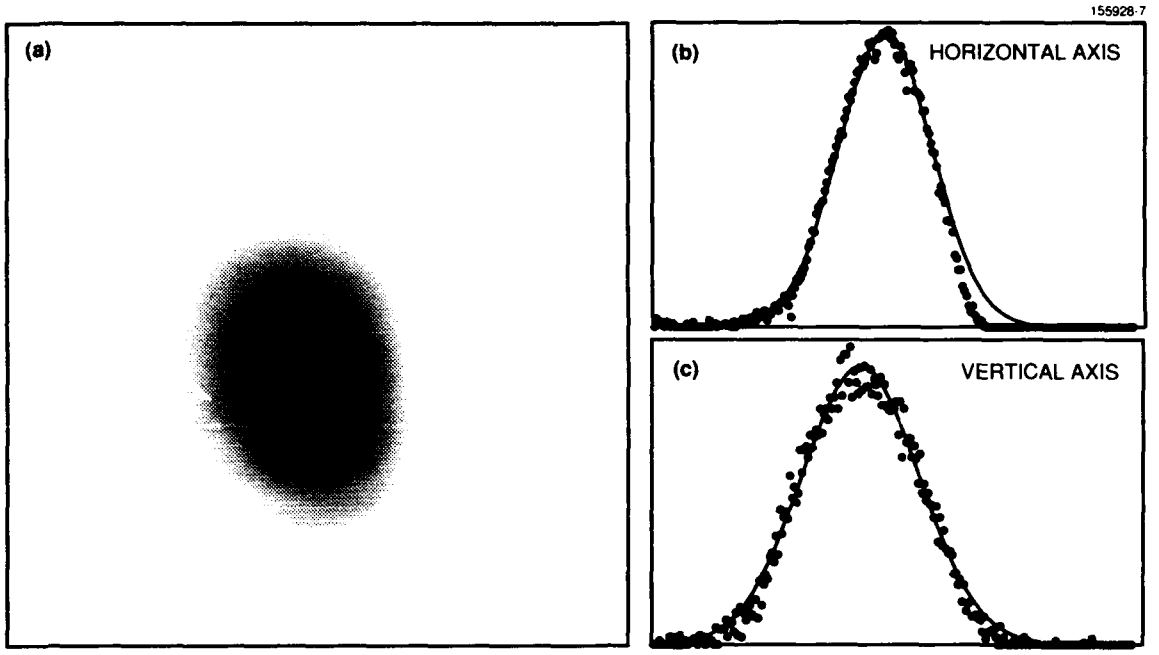

Figure 2-1. Near-field beam profile of the output of the Ti:Al_2O_3 master-oscillator/power-amplifier system. (a) Density plot in which the darker shading represents higher intensity. (b),(c) Profiles through the centroid of the data in the horizontal and vertical directions, respectively; the data are indicated by solid circles, and the solid lines are Gaussian fits to the data.

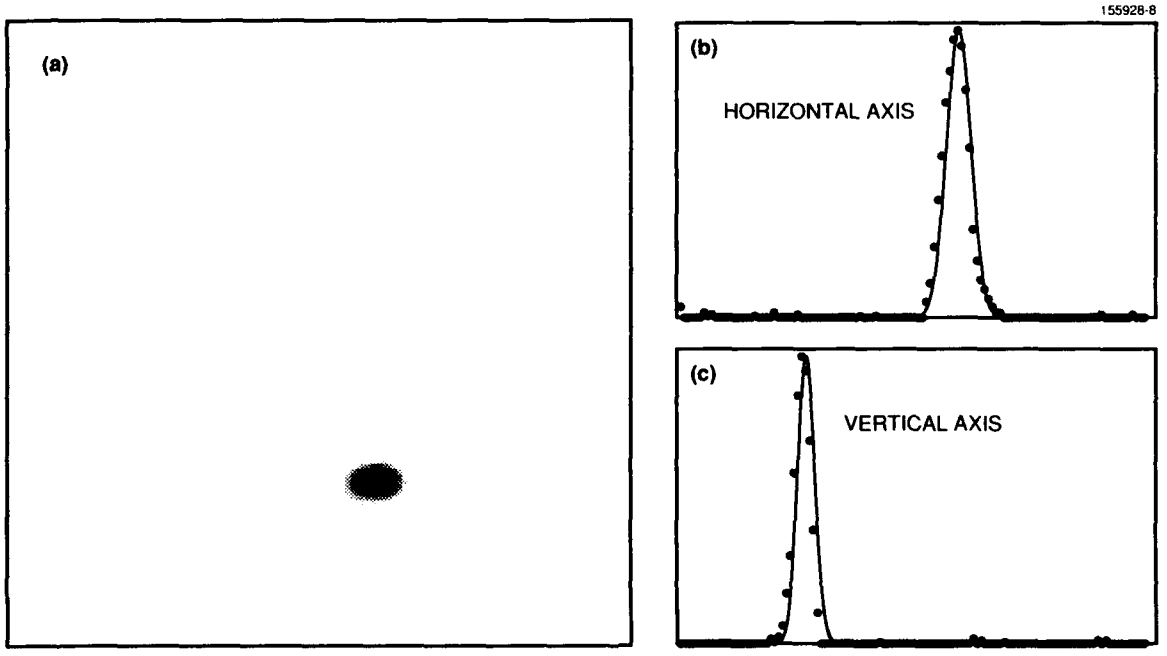

Figure 2-2. Far-field beam profile of the output of the Ti:Al_2O_3 master-oscillator/power-amplifier system that was obtained by focusing the output with a lens of 1-m focal length. (a) Density plot in which the darker shading represents higher intensity. (b),(c) Profiles through the centroid of the data in the horizontal and vertical directions, respectively; the data are indicated by solid circles, and the solid lines are Gaussian fits to the data.

the lens has a circularly symmetric Gaussian profile (a drawback of this method), the $1/e^2$ beam diameter d of the intensity is given by

$$d = a\sqrt{\frac{2}{\ln\left[I_0/\left(I_0 - I_t\right)\right]}}\ , \tag{2.1}$$

where a is the diameter of the pinhole, I_0 is the incident intensity, and I_t is the intensity transmitted through the pinhole. For a pinhole with $a = 520\ \mu$m we obtained $d = 424\ \mu$m, and for a pinhole with $a = 404\ \mu$m we obtained an average $d = 382\ \mu$m for two measurements. Taken together, the average value for the three measurements was $d = 396\ \mu$m. On the assumption of a collimated Gaussian beam of diameter D incident upon the lens, the diffraction-limited $1/e^2$ beam diameter $\mathcal{D}$ of the intensity is given by

$$\mathcal{D} = \frac{4}{\pi}\frac{f\,\lambda}{D}\ . \tag{2.2}$$

For D = 2.7 mm (the average of the horizontal and vertical values from Figure 2-1), the calculated value of $\mathcal{D}$ is 375 μm. The measured value was ~ 1.1 times the calculated value, and we conclude that the output of the Ti:Al_2O_3 MOPA is near diffraction limited.

In summary, the near-field output beam of the Ti:Al_2O_3 MOPA system can be characterized as elliptically Gaussian in nature. The far-field beam profile was also found to be elliptically Gaussian in nature. A measurement of the far-field nature of the output beam indicates that it is ~ 1.1 times the diffraction limit.

K.F. Wall
P.A. Schulz
R.A. Aggarwal
A. Sanchez
P. Lacovara
A. Walther
V. Daneu

2.2 FREQUENCY-MODULATED Nd:YAG LASER

Diode lasers are the usual choice for wide-bandwidth frequency-modulated optical sources, which are used in high-speed analog fiber-optic communication. However, diode-pumped solid state lasers such as Nd:YAG [2] have lower intensity noise at high frequency, and can also be amplified to the high power levels that are important for applications such as frequency-chirped coherent laser radar. This report describes a frequency-modulated Nd:YAG laser with a short-term frequency jitter of 300 kHz and frequency slew rates up to 25 MHz/ns with deviations from linearity of ~ 1 percent.

The Nd:YAG laser illustrated schematically in Figure 2-3 is housed by a 3-cm-thick disk of stainless steel. A $LiTaO_3$ electrooptic phase modulator tunes the laser over the longitudinal-mode separation of 20 GHz. The rigid design reduces acoustic vibration to ~ 0.1 nm, which is less than the interatomic spacing, as inferred from the short-term frequency jitter of 300 kHz. The laser operates in a single longitudinal mode because the Nd:YAG crystal is thin (1 mm) and placed at one end of the laser cavity.

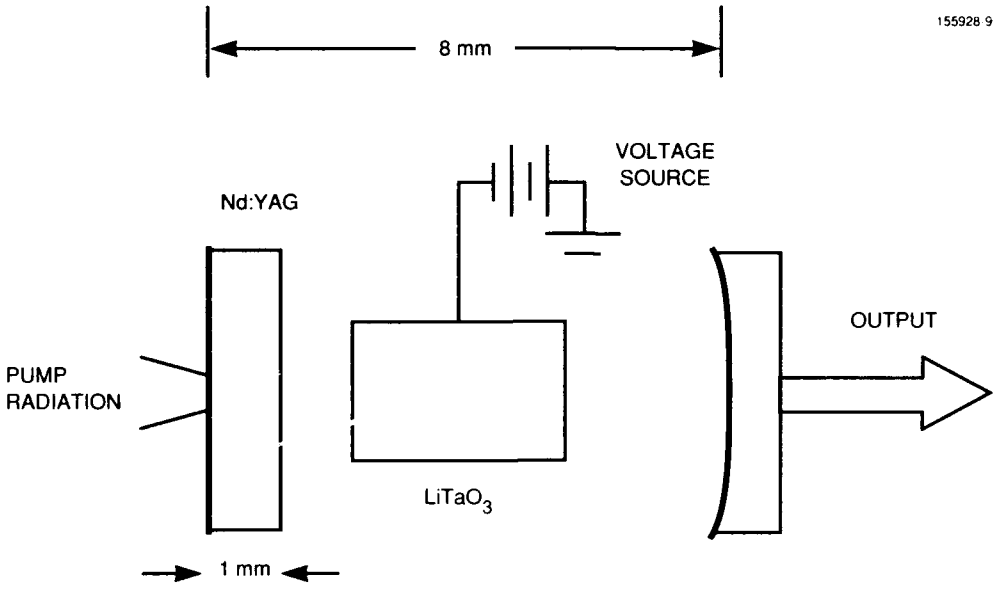

Figure 2-3. Schematic of Nd:YAG laser. Placing the 1-mm Nd:YAG gain medium at one end of the 8-mm-long laser cavity allows single-frequency operation at 2.5 times threshold. Tuning over the free spectral range of 20 GHz was obtained with a voltage change of 1.8 kV.

Thus, the walk-off of two cavity modes within the Nd:YAG crystal is small as long as the modes are within the Nd:YAG gain bandwidth. In this case, a second mode must compete for gain in the region where the first mode depletes the gain (spatial hole burning) rather than in the regions of undepleted gain. The laser runs in a single longitudinal mode at power levels that are higher (up to 2.5 times threshold) than they would be if the Nd:YAG crystal were longer or nearer the center of the cavity.

With a 5-percent output coupler, the laser generates 20 mW when pumped with 82 mW from a Ti:Al_2O_3 laser. Pumping the Nd:YAG laser with 200 mW of diode laser power produces only 4 mW of single-frequency output because the spectrum of the diode laser used is broad (2 nm) relative to the peak absorption spectral width (0.3 nm), resulting in less power absorbed over a longer distance. These power levels were found to be independent of the voltage applied to the $LiTaO_3$ crystal. The output coupler has a 5-cm radius of curvature, resulting in a stable laser cavity; because of this the laser beam parameters are only weakly dependent on the thermal lensing. This is in contrast to the microchip laser [3],[4] in which the thermal lens stabilizes the laser cavity making the beam diameter strongly dependent on the thermal lens.

The thin (1 mm) width of the $LiTaO_3$ in the z direction, across which voltage is applied, allows a large tuning range at low voltage with a sensitivity of 11 MHz/V. The small size of the crystal gives a

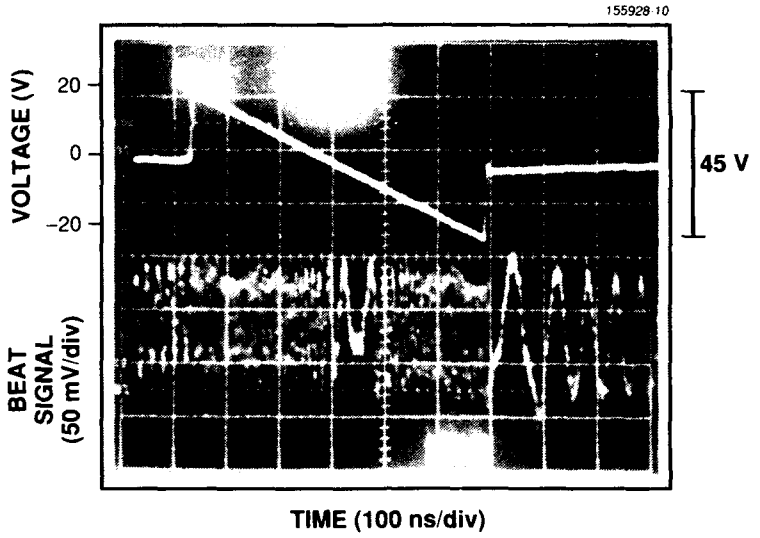

Figure 2-4. Heterodyne signal of a stable oscillator with a 500-MHz frequency-chirped oscillator. Upper trace shows the 570-ns voltage ramp applied to the $LiTaO_3$ crystal in the frequency-chirped oscillator cavity. Lower trace shows the resulting beat note measured with a fast photodiode. The results indicate that the modulator voltage causes linear frequency modulation of the laser output.

low capacitance and a good high-frequency response. The laser operates in a single polarization with $LiTaO_3$ in the cavity, but tends to run in both polarizations without it. The birefringence of the modulator crystal is responsible for the polarization selection. The frequently used electrooptic crystal $LiNbO_3$ is unsuitable in the present application because the photorefractive damage degrades the output power.

As the frequency of the applied voltage reaches ~ 1 MHz and above, acoustic resonances of the $LiTaO_3$ are excited, which cause undesired amplitude modulation of the output. To eliminate these resonances, lead and a sapphire-copper sandwich are bonded to the $LiTaO_3$ in the z and x crystal directions, respectively. These materials are acoustically impedance matched to the piezoelectrically excited acoustic modes of $LiTaO_3$. Acoustic waves are transmitted out of the electrooptic tuner and into the soft copper and lead, thus damping the amplitude modulation by more than an order of magnitude.

The frequency modulation capability was demonstrated by heterodyning the frequency-chirped oscillator with a single-frequency local oscillator. The beat signal resulting from a 45-MHz frequency offset appears in the first 140 ns, as seen in the lower trace of Figure 2-4. The frequency chirping was started with a step voltage change, which resulted in 250-MHz frequency switching in ~ 10 ns. The initial beat note chirped down to zero frequency after about 330 ns and then to –205 MHz by the end of the voltage sawtooth.

The linearity of the 570-ns, 500-MHz frequency chirp was studied by compressing the frequency-chirped beat note in a linearly dispersive surface acoustic wave device. Since this device has a center frequency of 1.3 GHz, the local oscillator frequency was offset by 1.3 GHz from the center frequency of the frequency-modulated laser. The ~ 1.3-GHz beat note was detected, amplified, and compressed to a 6-ns pulse. The frequency chirp nonlinearity is 1 percent, as obtained from the ratio of the 6-ns compressed pulse to the 570-ns chirp time.

S.R. Henion
P.A. Schulz

2.3 ROLE OF ENERGY DIFFUSION IN DETERMINING THE LIMITS OF SINGLE-MODE OPERATION OF STANDING-WAVE LASERS

Spatial hole burning and energy diffusion are responsible for shaping the population inversion in standing-wave laser cavities. The spatial distribution of the population inversion determines the gain of the different cavity modes and, therefore, which modes will lase. Here, we derive analytic expressions that give the ratio of the maximum single-longitudinal-mode inversion density to the threshold inversion density for a standing-wave laser in the presence of energy diffusion. This treatment is intended to complement the treatment of spatial hole burning given earlier [5]. The results are written in terms of the cavity geometry and material parameters, and can serve as a practical guideline in the design of single-frequency lasers.

Following the approach of Reference 5, we consider a CW standing-wave laser cavity containing a homogeneously broadened gain medium of length ℓ and make the assumption that the round-trip loss of the cavity is relatively low, allowing the development of a well-defined standing-wave intensity pattern. By making a plane-wave approximation for the transverse mode profile, the intensity of mode m within the gain media can be written as

$$I_m(z) = 4I_m \sin^2\left(k_m z + \theta_m\right) , \tag{2.3}$$

where I_m is the intensity of the beam traveling in one direction within the laser cavity, k_m and θ_m are determined by the geometry of the cavity, and z is the dimension along the cavity axis. For a cavity with the gain media located between $z = 0$ and $z = \ell$ we can write the CW rate equations for each of the oscillating modes as

$$\sigma_m \int_0^{\ell} N(z) I_m(z) dz = \gamma_m I_m , \tag{2.4}$$

and the rate equation for the inversion density $N(z)$ as

$$P(z) = \sum_m \frac{\sigma_m N(z) I_m(z)}{\hbar\omega_m} + \frac{N(z)}{\tau_{\text{eff}}} - D\frac{d^2 N(z)}{dz^2} , \tag{2.5}$$

where σ_m is the value of the emission cross section at the frequency ω_m corresponding to mode m, γ_m is the total round-trip loss for mode m (including transmission through the cavity mirrors), $P(z)$ is the pump rate, τ_{eff} is the effective relaxation time for the inversion density in the absence of stimulated emission, and D is the energy diffusion constant [6]. The condition for single-mode operation is

$$\int_0^\ell N(z)\left[I_2(z)/I_2 - \beta(1,2)I_1(z)/I_1\right]dz < 0 \ , \tag{2.6}$$

where the discrimination factor $\beta(1,2)$ is given by

$$\beta(1,2) \equiv \frac{\sigma_1 \gamma_2}{\sigma_2 \gamma_1} \ , \tag{2.7}$$

and the indices 1 and 2 correspond to the first and second mode to lase. What remains is to solve Equation (2.5) for $N(z)$.

Equation (2.5) cannot be solved in closed form. However, by considering a worst case scenario we can derive an estimate for how far above threshold a standing-wave laser will oscillate in a single longitudinal mode in the presence of energy diffusion. Imagine that the gain medium is inverted only at the nulls in the optical field of the first cavity mode to lase. This creates a favorable situation for a second oscillating mode since the first mode is unable to deplete the gain at these locations. This is, in fact, the type of population inversion profile that is obtained in the limit of strong spatial hole burning. After the initial (imaginary) inversion, energy diffusion will spread out the inverted population. If we assume a uniform diffusion length L_D (to be determined self-consistently later), the steady state inversion distribution within the gain media becomes

$$N(z) = \sum_n N_n \exp\left[-\left|\left(z - z_n\right)/L_D\right|\right] \ , \tag{2.8}$$

where z_n is the position of a null in the optical field of the first mode to lase and N_n is related to the excitation by

$$\int_{-\infty}^{+\infty} N_n \exp\left[-\left|\left(z - z_n\right)/L_D\right|\right]dz = \alpha \int_{z_n - \lambda_1/4}^{z_n + \lambda_1/4} N_0(z)dz \ , \tag{2.9}$$

in which λ_1 is the wavelength of the first lasing mode, α is independent of z, and $N_0(z) = \tau_{eff}P(z)$ is the inversion in the absence of saturation.

With the use of (2.8), the condition for single-mode operation given in (2.6) becomes

$$\frac{\beta(1,2) - 1}{1 - \langle \psi(1,2) \rangle} > \frac{1}{4{k_1}^2 {L_D}^2} \ , \tag{2.10}$$

where $\langle \psi(1,2) \rangle$ is given by

$$\langle \psi(1,2) \rangle \equiv \frac{1}{\ell \langle N \rangle} \int_0^\ell N_0(z) \cos\left[2\left(k_1 - k_2\right)z + 2\left(\theta_1 - \theta_2\right)\right]dz \tag{2.11}$$

and

$$\langle N \rangle = \frac{1}{\ell} \int_0^{\ell} N_0(z)\, dz \ . \tag{2.12}$$

It has been assumed that ℓ is much greater than $1/k_1$ and that $N_0(z)$ changes much more slowly with z than $\sin^2(k_1 z)$. All that remains now is to determine the diffusion length L_D.

For material with a uniform diffusion coefficient D and a uniform relaxation time τ the diffusion length is given by

$$L_D{}^2 = \tau D \ . \tag{2.13}$$

For the actual case, however, the lifetime of the population inversion has a spatial dependence owing to the effects of stimulated emission, and is given by

$$\frac{1}{\tau} = \left[\frac{I(z)}{I_{\text{sat},1}} + 1 \right] \frac{1}{\tau_{\text{eff}}} \ , \tag{2.14}$$

where

$$I_{\text{sat},1} = \frac{\hbar \omega_1}{\sigma_1 \tau_{\text{eff}}} \ . \tag{2.15}$$

This spatial dependence is exactly what leads to spatial hole burning. To account for this, we will use the expected value of the inverse lifetime, which is given by

$$\langle 1/\tau \rangle = \frac{1}{\alpha \ell \langle N \rangle} \int_0^{\ell} N(z)/\tau \, dz \ , \tag{2.16}$$

where the value of $1/\tau$ used in Equations (2.13) and (2.8) to define $N(z)$ is the mean value $\langle 1/\tau \rangle$. The self-consistent solution to Equation (2.16) is

$$\frac{1}{\langle 1/\tau \rangle} = \left(\left[\frac{\tau_{\text{eff}}}{2} - \frac{1}{8 k_1{}^2 D} \right] + \left[\left(\frac{\tau_{\text{eff}}}{2} - \frac{1}{8 k_1{}^2 D} \right)^2 + \frac{\tau_{\text{eff}}}{4 k_1{}^2 D} \left(\frac{2I_1}{I_{\text{sat},1}} + 1 \right) \right]^{1/2} \right) \left(\frac{2I_1}{I_{\text{sat},1}} + 1 \right)^{-1} \ . \tag{2.17}$$

Physically, this equation is reasonable. For small amounts of spatial hole burning, or large amounts of energy diffusion, the expected value of the inverse lifetime of the population inversion is just the spatially averaged value of the inverse lifetime throughout the gain medium. In the presence of strong spatial hole burning, the excited states are localized near the nulls in the optical field, and the expected value of the inverse lifetime is smaller than the spatially averaged value, since most of the inverted population is not exposed to the strong, stimulating optical fields.

Using (2.17) and the fact that above threshold

$$\frac{2I_1}{I_{\text{sat},1}} \le \frac{\langle N \rangle}{N_{\text{thresh}}} - 1 \ , \tag{2.18}$$

where $N_{\text{thresh}} = \gamma_1 / 2\sigma_1 \ell$, we can rewrite (2.10) as

$$\langle N \rangle < \zeta_D(1,2) N_{\text{thresh}} \quad , \tag{2.19}$$

in which

$$\zeta_D(1,2) \equiv \left(4k_1^2 D\tau_{\text{eff}} - 1\right)\left(\frac{\beta(1,2)-1}{1-\langle\psi(1,2)\rangle}\right) + 4k_1^2 D\tau_{\text{eff}}\left(\frac{\beta(1,2)-1}{1-\langle\psi(1,2)\rangle}\right)^2 \quad . \tag{2.20}$$

Expression (2.19) is the main result of this report.

The model developed here is not an accurate model near threshold in a gain medium with little energy diffusion. In this situation, energy diffusion is not important, and spatial hole burning is all that needs to be considered. The previously derived result [5],

$$\langle N \rangle < \zeta_{SH}(1,2) N_{\text{thresh}} \quad , \tag{2.21}$$

where $\zeta_{SH}(1,2)$ is the ratio of the maximum single-mode inversion density to the threshold inversion density in the absence of energy diffusion and is given by

$$\zeta_{SH}(1,2) \equiv \left(\frac{\beta(1,2)-1}{1-\langle\psi(1,2)\rangle} + 1\right)\left(\frac{2[\beta(1,2)-1]}{1-\langle\psi(1,2)\rangle} + 1\right) , \tag{2.22}$$

should be very accurate. The model developed in this report becomes increasingly accurate as spatial hole burning leads to strong localization of the inverted population on the scale set by energy diffusion. This is the region where energy diffusion is important, and (2.21) is no longer expected to be accurate. Whichever relation, (2.19) or (2.21), predicts the larger single-mode inversion ratio will be the better estimate of the maximum single-mode value of $\langle N \rangle / N_{\text{thresh}}$. For this reason, it makes sense to define a maximum inversion ratio $\zeta(1,2)$ as the larger of $\zeta_D(1,2)$ and $\zeta_{SH}(1,2)$. The quantity $\zeta(1,2)$ is shown as a function of $[\beta(1,2)-1]/[1-\langle\psi(1,2)\rangle]$ for several values of $4k_1^2 D\tau_{\text{eff}}$ in Figure 2-5.

J.J. Zayhowski

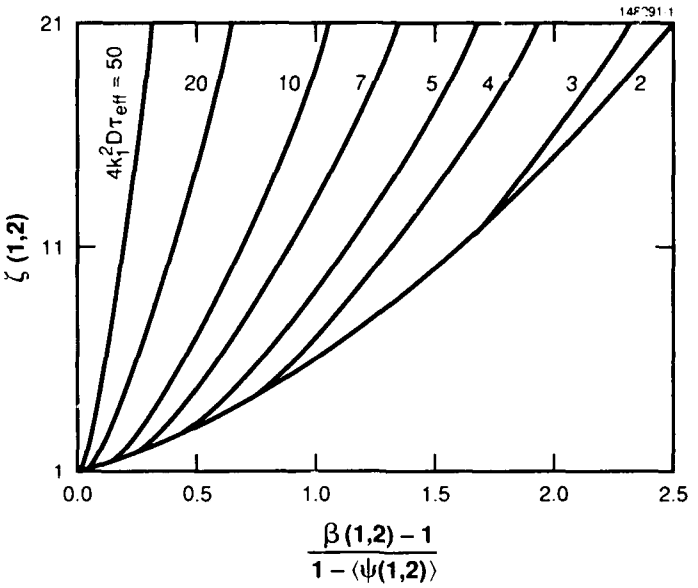

Figure 2-5. $\zeta(1,2)$ as a function of $[\beta(1,2)-1]/[1-\langle\psi(1,2)\rangle]$ for several values of $4k_1^2D\tau_{eff}$.

2.4 THERMAL STABILIZATION OF MICROCHIP LASER CAVITIES

Microchip lasers use a plane-parallel laser cavity and rely on thermal focusing in the gain medium to define the oscillating mode diameter [3],[4]. As a result, only gain media with positive thermal lensing are potential candidates for microchip lasers. In addition, for such gain media the parallelism of the mirrors must be very good; for Nd:YAG, for example, the tolerance in mirror misalignment is typically a few microradian [3],[7]. These requirements on the gain media and the parallelism of the mirrors could be greatly reduced if one of the cavity mirrors is curved, or if a lens is introduced into the cavity. However, optical components with curved surfaces usually require individual handling and are, therefore, more costly than flat components. As an alternative, we have introduced a thin, flat piece of GaAlAs within the microchip laser cavity to act as a thermal lens, and thereby stabilize the cavity.

The microchip laser used in the experiments reported here was created from a 640-μm-thick piece of Nd:YAG polished flat and parallel. The pump surface of the Nd:YAG was dielectrically coated to be highly reflecting at 1.064 μm while transmitting the pump light. The opposite surface was antireflection coated for 1.064-μm light, so that a separate output coupler could be used. A flat output coupler, with 0.3-percent transmission at the lasing wavelength, was placed about 300 μm from the Nd:YAG, as shown in Figure 2-6. The laser was then pumped with 300 mW of 808-μm radiation from a Ti:Al_2O_3 laser. The output coupler was intentionally misaligned, resulting in an output beam with the far-field profile shown in Figure 2-7. A 150-μm-thick piece of GaAlAs, polished flat and parallel, was then intro-

duced into the laser cavity between the Nd:YAG and the output coupler (see Figure 2-6). The GaAlAs absorbed the portion of the pump power transmitted by the Nd:YAG, while transmitting the light at 1.064 μm. This residual pump power created a thermal lens which stabilized the cavity, and resulted in an output beam with the far-field pattern shown in Figure 2-8.

J.J. Zayhowski
R.C. Hancock

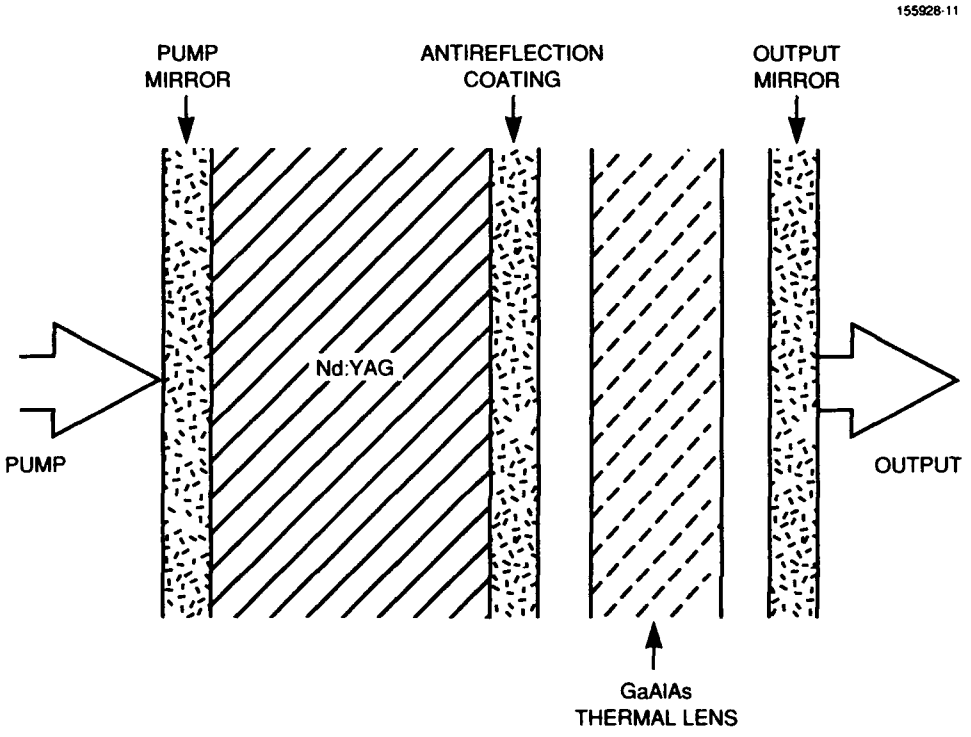

Figure 2-6. Illustration of a microchip laser cavity with a separate output coupler, showing the position of the GaAlAs thermal lens.

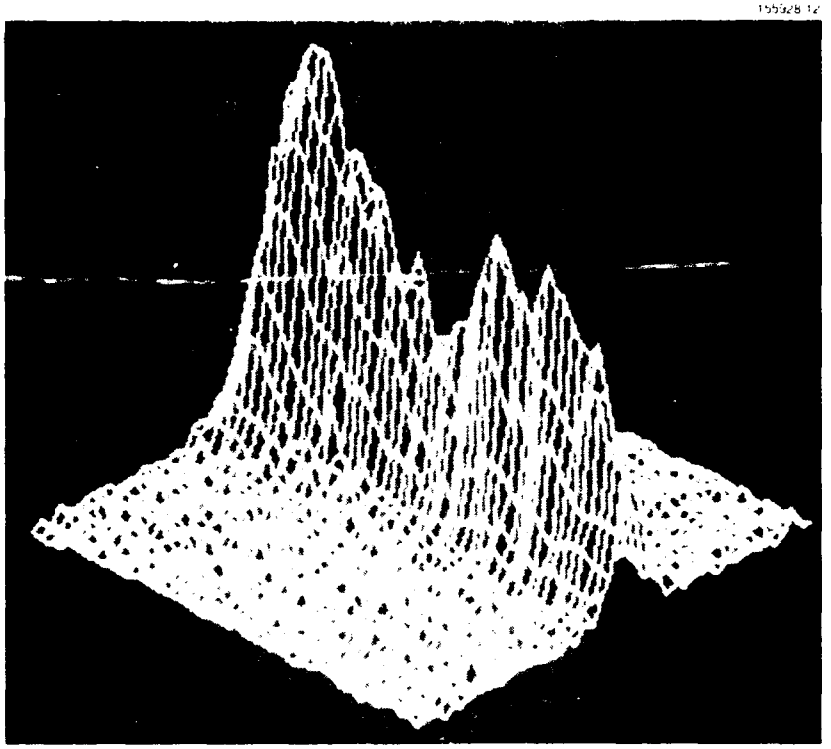

Figure 2.7 Far-field profile of a monolithic microchip laser.

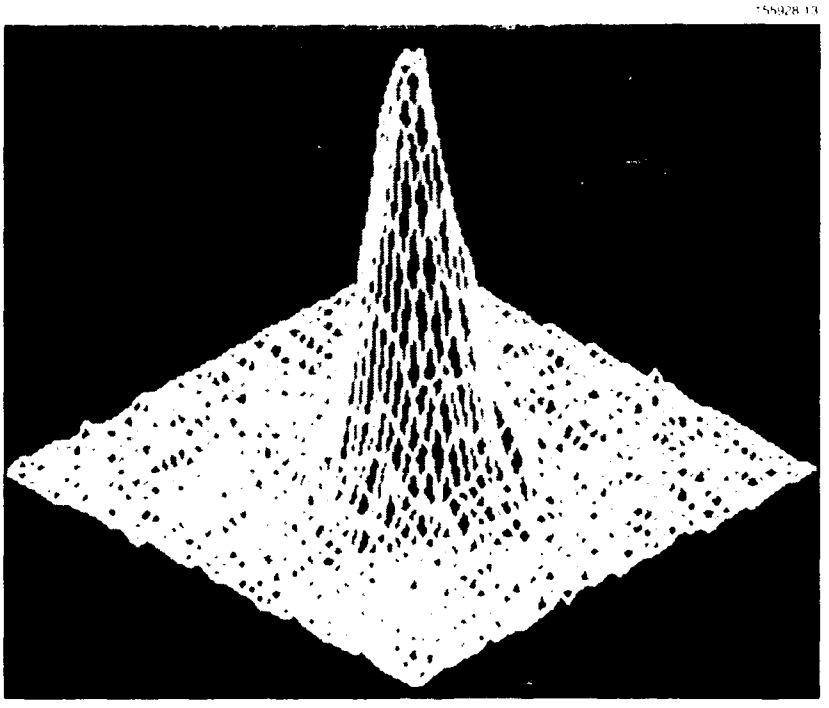

Figure 2.8 Far-field profile of a monolithic [illegible] containing a thin slice of GaAlAs.

2.5 TECHNIQUE FOR MASS PRODUCING TWO-DIMENSIONAL ARRAYS OF MONOLITHIC SOLID STATE LASER CAVITIES WITH CURVED MIRRORS

Laser cavities with curved mirrors are more stable than plane-parallel laser cavities and impose fewer restrictions on the gain media [8]. The disadvantage of curved mirror cavities is that they are normally more expensive to produce. Here, we report a method for inexpensively mass producing two-dimensional arrays of monolithic solid state lasers with curved mirrors.

The arrays are produced using a four-step process. First, wafers of gain media are cut to the desired thickness and polished flat and parallel, as illustrated in Figure 2-9(a). The thickness of the wafer corresponds to the cavity length of the laser. Second, the polished wafer is scribed in a grid pattern (on one or both surfaces) as shown in Figure 2-9(b). For this purpose we use a dicing saw with a blade thickness of 500 μm and scribe the wafer to a depth of 75 μm. The width and depth of the scribe must be sufficient to allow flow of the polishing slurry used in step three. The distance between the scribe marks defines the transverse dimensions of the laser cavity. Third, the scribed wafer is again polished. During polishing a natural rounding is produced by the deformation of the polisher and by the buildup of slurry under the edges of each element, as shown in Figure 2-9(c). The amount of rounding is determined by several factors including the type of polisher, the type of slurry, the amount of force applied to the crystal, and the polishing time. Each of these factors can be controlled to produce the desired amount of curvature. Wax polishers, for example, create small amounts of rounding compared to most pad-type polishers. Fourth, the wafer is dielectrically coated to create the proper-reflectivity mirrors, as seen in Figure 2-9(d). Finally, as an optional step, the array can be cut into individual laser cavities by cutting along the center of the scribed channels, as shown in Figure 2-9(e). This eliminates surface distortion that could otherwise occur from relieving strains in the surface of the crystal during the cutting operation.

Using the procedure outlined above we have created arrays of 1-mm-long, monolithic Nd:YAG lasers with one curved mirror whose radius varies from 50 cm to 4 m, and one flat mirror. The surface figure of the curved mirror was better than $\lambda/50$ (at $\lambda = 1.064$ μm). The surfaces with a 4-m radius of curvature were obtained by using a wax polisher and colloidal silica, with a force of 0.15 kg/cm^2 applied downward on the Nd:YAG for 8 h. An interferogram (514-nm light) and a surface profile of the resulting surface are shown in Figure 2-10. The irregular shape of the section shown in Figure 2-10(a) is a result of chipping by the dicing saw. Recent changes in the scribing procedure have greatly reduced the amount of chipping, resulting in maximum chip dimensions of less than 20 μm. The lighter areas of the interferogram, near the edges of the polished region, correspond to the thinner portions of the crystal. The surface profile shown in Figure 2-10(b) was taken over an 800-μm path, passing though the center of the crystal. Traces taken at different positions, and in different directions, are consistent with a spherical surface of 4-m radius, to within 0.01 μm, out to a distance of 400 μm from the center of the crystal. This curvature results in a fundamental-mode waist size of 140 μm for lasing at 1.064 μm, which is well matched to the pump field of a butt-coupled diode laser.

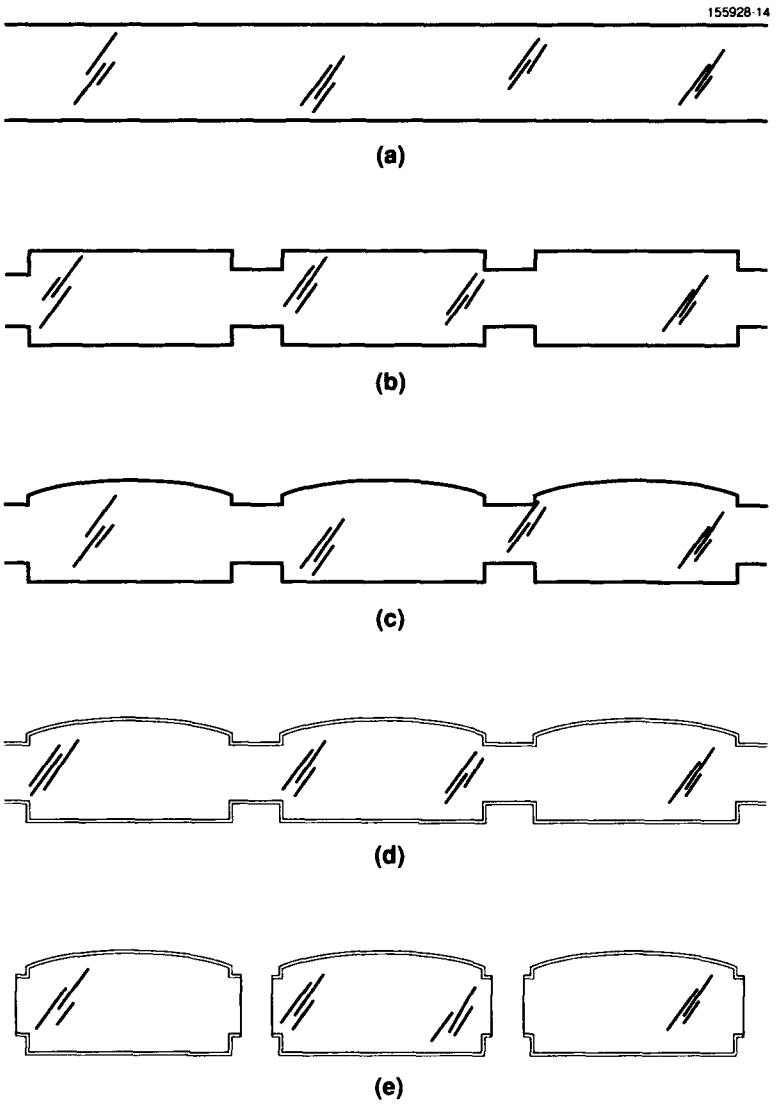

Figure 2-9. Steps in producing an array of monolithic, curved-mirror solid state laser cavities. Shown are cross sections of (a) a wafer of gain medium that has been polished flat and parallel, (b) a polished wafer scribed to define individual laser cavities, (c) a scribed wafer polished to produce curved surfaces, (d) a wafer dielectrically coated to create cavity mirrors, and (e) a wafer cut into individual laser cavities.

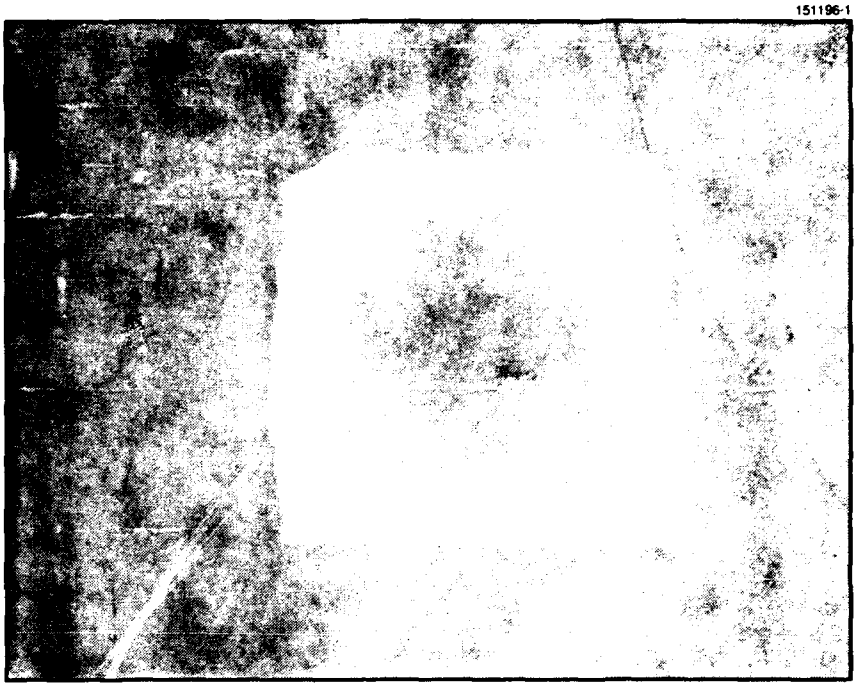

(a)

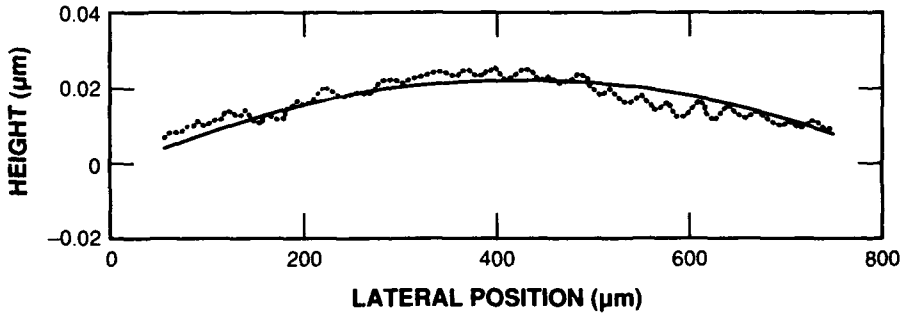

(b)

Figure 2-10. 1-mm-square surface with a 4-m radius of curvature. (a) Interferogram obtained by using 514-nm light. (b) Measured surface profile (dotted line) and ideal surface profile (solid line).

Surfaces with a shorter radius of curvature were obtained by using a pad with a spongy backing, colloidal silica, and a force of 0.15 kg/cm^2. A 50-cm radius of curvature was reached after 8 h of polishing. An interferogram (514-nm light) and a surface profile of the resulting surface are shown in Figure 2-11. The interferogram shows three interference fringes, which become circularly symmetric near the center of the crystal. The surface profile shown in Figure 2-11(b) was again taken over an 800-μm path, passing through the center of the crystal. Traces taken at different positions, and in different directions, are consistent with a spherical surface of 50-cm radius, to within 0.02 μm, out to a distance of 400 μm from the center of the crystal. An interferogram of an array of surfaces with a 50-cm radius of curvature is shown in Figure 2-12. The optical flat used to obtain this interferogram was held at a slight angle to the surface of the Nd:YAG crystals. These laser cavities have a fundamental-mode waist size of 85 μm at 1.064 μm, and they can easily be pumped with the focused output of a single diode laser or with a spatially multiplexed array of diode lasers [9].

J.J. Zayhowski
J.L. Daneu

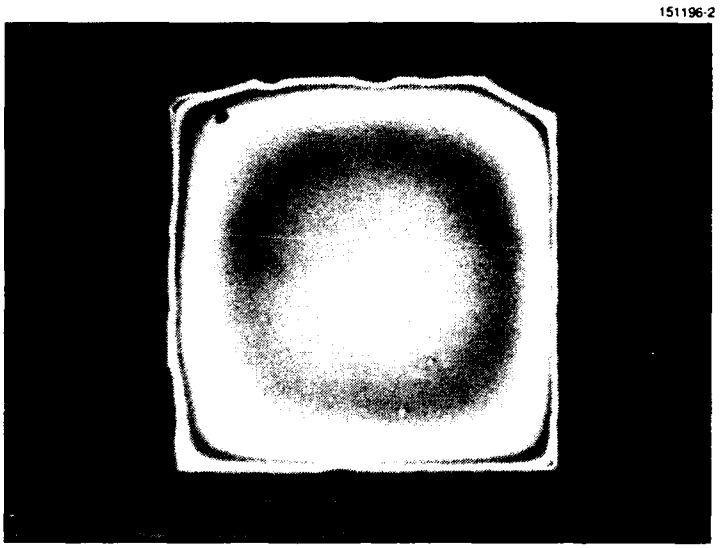

(a)

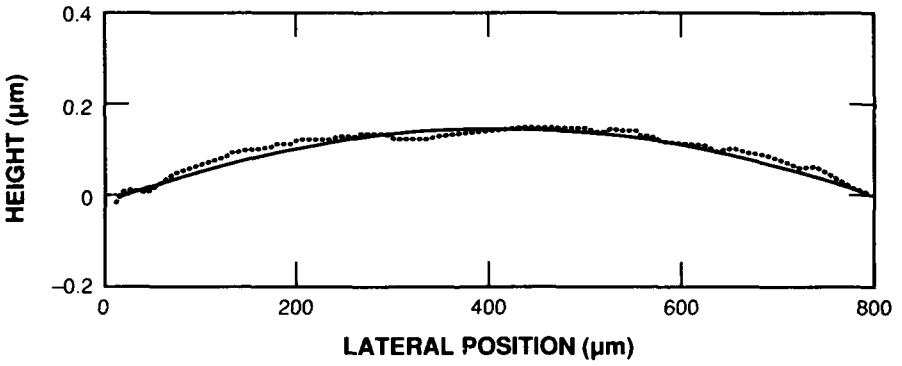

(b)

Figure 2-11. 1-mm-square surface with a 50-cm radius of curvature. (a) Interferogram obtained by using 514-nm light. (b) Measured surface profile (dotted line) and ideal surface profile (solid line).

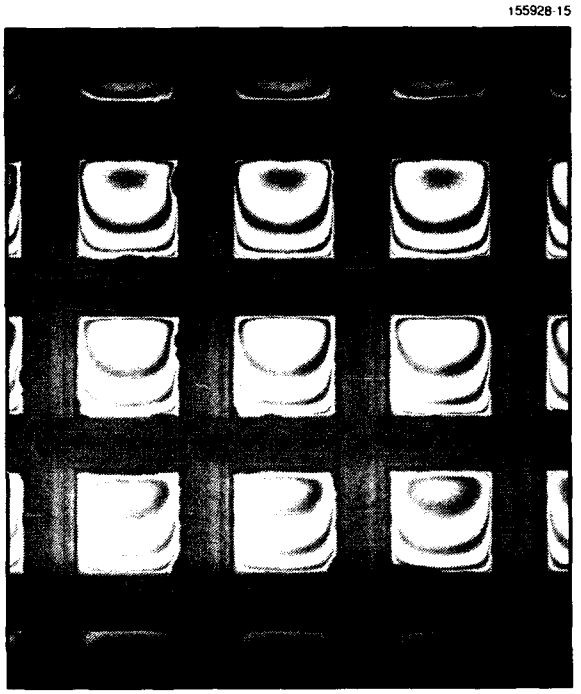

Figure 2-12. Interferogram of an array of surfaces with a 50-cm radius of curvature.

2.6 SUM-FREQUENCY GENERATION IN TANDEM $LiIO_3$ CRYSTALS

A theoretical study by Volosov et al. [10] of second-harmonic generation (SHG) in nonlinear crystals arranged in tandem indicates that, if the crystals are properly oriented relative to each other and to the input beam, competing parametric processes are suppressed and the acceptable phase mismatch is increased. The latter effect is equivalent to increasing the phase-matching acceptance angle for frequency conversion. This factor is particularly germane for improved frequency conversion in $LiIO_3$, which has an extremely small phase-matching acceptance angle of ~ 3 mrad cm full width at half-maximum (FWHM) for SHG at 1.06 μm. Results of SHG experiments carried out by Andreev et al. [11] using a series of tandem crystals of $LiIO_3$ and CsH_2AsO_4 (CDA) are in general agreement with the theoretical predictions. We have extended the experimental study to consideration of sum frequency generation (SFG) with two crystals placed in tandem. Our initial experiments were carried out with two Nd:YAG Quantronix lasers, one operating at 1.32 μm and the other at 1.06 μm in order to generate yellow light at 0.589 μm. Both lasers operated Q switched with a 5-kHz pulse repetition frequency. The first $LiIO_3$ crystal was 20 mm long and antireflection coated at both ends in the infrared; the second $LiIO_3$ crystal was 12 mm long and uncoated.

With each of the laser inputs fixed at an average power of 200 mW, the beams were made collinear and focused through a 560-mm cylindrical lens onto the $LiIO_3$ crystals. The SFG (average power) of the individual crystals was 1.02 mW from the 20-mm crystal and 0.3 mW from the 12-mm crystal. However, with the 12-mm crystal placed in series with the 20-mm crystal, 1.9-mW SFG was obtained. The achievement of a tandem SFG output greater than the sum of the individual outputs can only be explained by an increased acceptance angle and indicates that the analysis used for SHG has direct application to the frequency summing process.

The sum-frequency-mixing experiment was repeated with the Quantel Nd:YAG pulsed laser system [12]. The laser outputs of this system are long pulsed ($\tau_p \approx 100\ \mu s$) and mode locked. The system operates at a 10-Hz pulse repetition frequency and produces average power outputs of up to 8 W at 1.06 μm and 6.7 W at 1.32 μm. The use of this system enabled us to extend the study to high power and efficiency levels.

The SFG of the two crystals in tandem never exceeded the sum of the SFG of the individual crystals. At input power levels $P(1.06) = P(1.32) = 2$ W, the addition of the second crystal (12 mm long) increased the 0.589-μm output from 0.4 to 0.5 W. The failure to exceed the sum of the individual crystal outputs at the lower input power levels with the Quantel system is believed to be due to the reduced divergence of the laser beams of the pulsed system relative to those of the Q-switched system. The fractional improvement due to the presence of the second crystal decreased with increasing input power levels. At the highest attainable input levels the sum frequency output was approximately the same with or without the second crystal [$P(0.589) = 4$ W], indicating pump depletion. Since the second crystal was uncoated, its contribution even at the highest input level was sufficient to overcome Fresnel losses due to reflection at its surfaces. Hence, with antireflection-coated surfaces, a gain of approximately 20 percent at the highest input level is anticipated, with the possibility of still further gains by using additional crystals.

N. Menyuk
J. Korn

REFERENCES

1. Solid State Research Report, Lincoln Laboratory, MIT (1990:1), p. 9.
2. T.J. Kane, *IEEE Photon. Technol. Lett.* **2**, 244 (1990).
3. J.J. Zayhowski, to be published in *OSA Proc. Advanced Solid State Lasers* (Optical Society of America, Washington, D.C., 1990).
4. Solid State Research Report, Lincoln Laboratory, MIT (1989:4), p. 26.
5. J.J. Zayhowski, *Opt. Lett.* **15**, 431 (1990); Solid State Research Report, Lincoln Laboratory, MIT (1989:4), p. 23.

6. H.G. Danielmeyer, in *Lasers*, A.K. Levine and A.J. DeMaria, eds. (Marcel Dekker, New York, 1976), Vol. 4, p. 1.

7. Solid State Research Report, Lincoln Laboratory, MIT (1989:4), p. 29.

8. Solid State Research Report, Lincoln Laboratory, MIT (1990:2), p. 20.

9. T.Y. Fan, A. Sanchez, and W.E. DeFeo, *Opt. Lett.* **14**, 1057 (1989).

10. V.D. Volosov, A.G. Kalintsev, and V.N. Krylov, *Sov. J. Quantum Electron.* **6**, 1163 (1976).

11. R.B Andreev, K.V. Vetrov, V.D. Volosov, and A.G. Kalintsev, *Opt. Spektrosk.* (USSR) **63**, 793 (1987).

12. Solid State Research Report, Lincoln Laboratory, MIT (1989:4), p. 18.

3. MATERIALS RESEARCH

3.1 HORIZONTAL GRADIENT-FREEZE GROWTH OF InP CRYSTALS UNDER CONTROLLED PRESSURE

Indium phosphide substrates with ideal properties for the fabrication of high-power and very high frequency electronic and optoelectronic devices are not yet available. Currently, most bulk InP crystals for research and commercial applications are grown by the liquid-encapsulated Czochralski (LEC) method, but doping nonuniformity, high defect density, and brittleness due to residual strain are serious problems. As an alternative, we are investigating the use of a horizontal gradient-freeze (HGF) method employing a sealed pressure-balanced system for synthesis and in situ crystal growth of InP without melt encapsulation. Such a method can be expected to yield crystals with low dislocation densities, like InP and GaAs grown by the vertical gradient-freeze method [1] and GaAs grown commercially by the HGF method, as well as to eliminate the impurity contamination that can accompany transfer of synthesized material to a separate growth system. In addition, since the melt is not encapsulated, the P pressure can be adjusted to obtain the optimum melt composition for minimizing defect density, impurity contamination, and twinning.

The pressure-balanced system was developed in order to permit the explosion-free synthesis of InP at P vapor pressures up to or even beyond the value of 25 atm that is in equilibrium with stoichiometric InP at the maximum melting point. In our conventional procedure for InP synthesis, In in a fused silica boat is loaded into one end of a long silica ampoule and excess red P is loaded into the other end. The ampoule is evacuated, sealed and placed in a horizontal furnace that has separate windings for independently heating the two ends. The In is melted and heated to ~ 1050°C, with the temperature along the boat decreasing toward the center of the ampoule. The P is heated to a lower temperature, typically 465°C, generating P vapor that is dissolved into the molten In. After the melt has been saturated with P, the ampoule is pulled through the furnace at a rate of 2 to 5 cm per day to directionally solidify InP, starting at the cooler end of the boat.

Several problems are encountered in using this synthesis technique. The maximum P pressure is limited by the strength of the silica ampoule to about 15 atm. Furthermore, the pressure-temperature curve can vary significantly from batch to batch of red P, particularly from different suppliers, and the pressure can also change with time. Therefore, controlling the temperature of the P reservoir at a fixed value does not provide a melt with known or even constant composition. A number of ampoules have exploded violently in the midst of a run, even though the P pressure is expected to be only about 7 atm at 465°C, while in some runs the pressure has been so low that very little P was transported into the boat.

To solve these problems, we have constructed a horizontal system in which the synthesis ampoule containing the In boat and P reservoir is placed inside a steel high-pressure vessel, and the P pressure inside the ampoule is automatically matched to whatever inert gas pressure is established outside the ampoule. Figure 3-1 shows a schematic cross-sectional diagram of this system, with a loaded ampoule in place, together with the temperature profile along the axis of the system at the beginning of growth. A fused silica diaphragm is incorporated at the P end of the ampoule to sense the difference between the

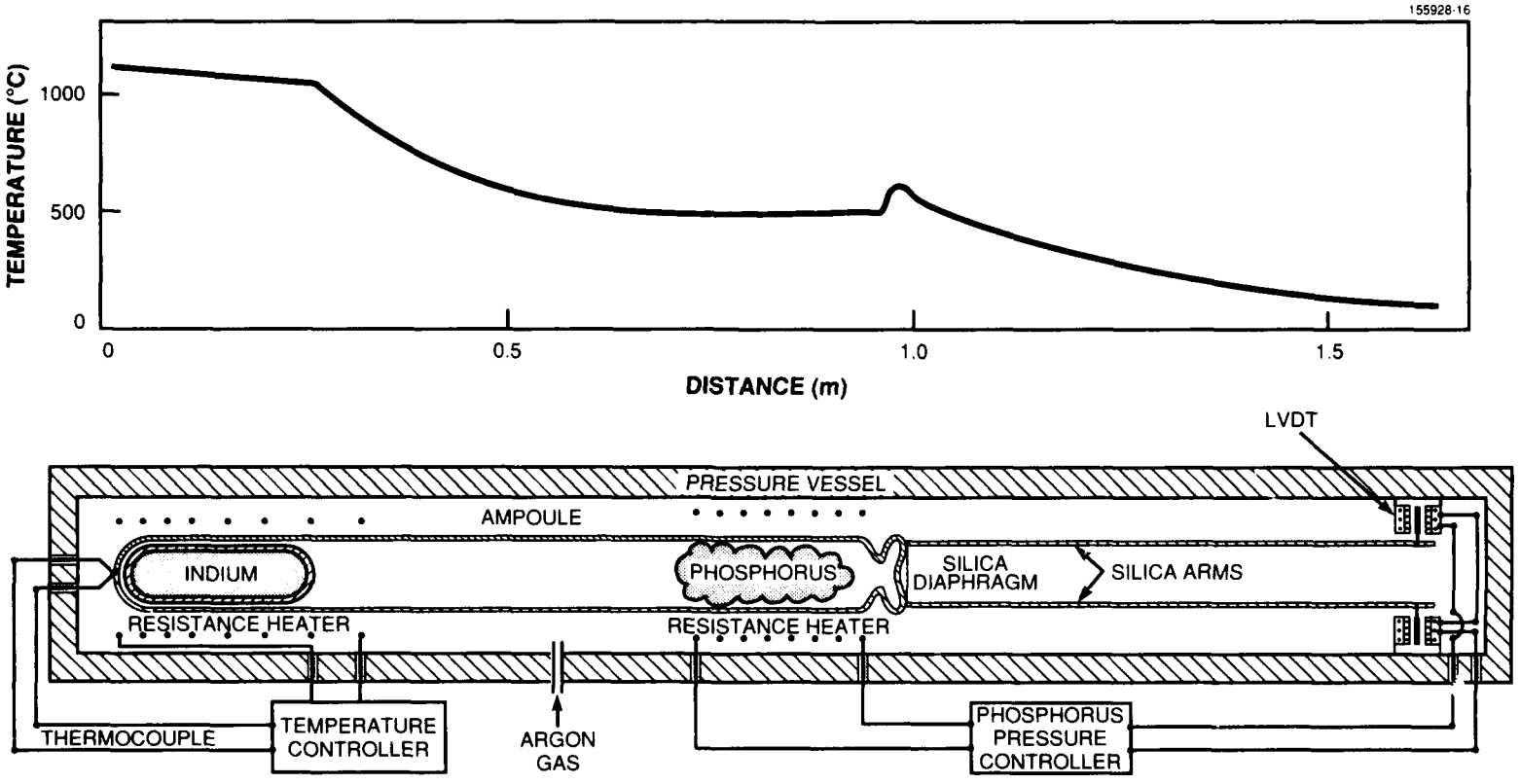

Figure 3-1. System for synthesis and in situ horizontal gradient-freeze growth of InP: schematic cross-sectional diagram and temperature profile along the axis of the ampoule.

internal and external pressures, and two long fused silica arms are attached to the diaphragm. A voltage that depends on the flexure of the diaphragm is generated by means of linear variable differential transformers (LVDTs) mounted at the ends of the silica arms. This voltage is used as the input signal to a controller that adjusts the power to the P reservoir heater, thereby fixing the P pressure. Figure 3-2 is a photograph of a loaded ampoule showing the two arms, and Figure 3-3 is a photograph of a diaphragm that has been cut in half to show its structure.

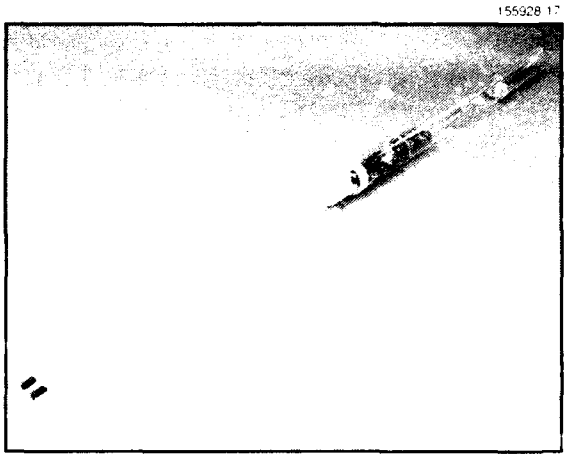

Figure 3-2. Sealed synthesis, growth ampoule containing In and P.

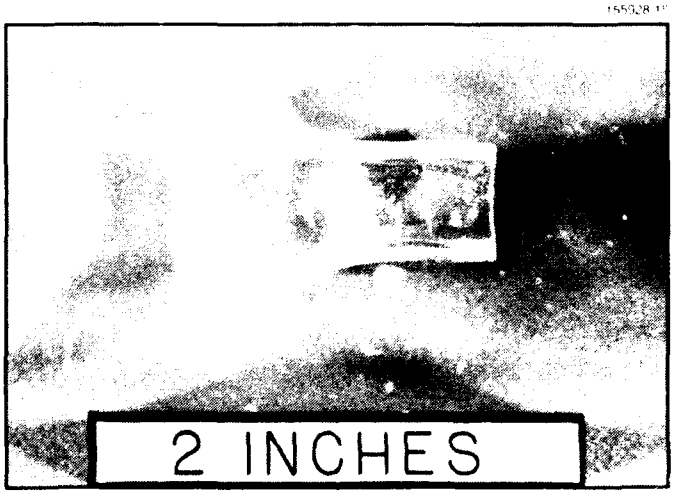

Figure 3-3. Pressure-sensing silica diaphragm that has been cut in half to show its structure.

At the beginning of a run, the ampoule and pressure vessel are both under vacuum. The temperatures of the In boat and the diaphragm are first raised to the temperatures shown in Figure 3-1. Then the temperature of the P reservoir is slowly increased to begin generating P vapor, and at the same time Ar gas is admitted to the pressure vessel. By initially adjusting the controller so that the input voltage generated by the LVDTs is maintained at the value obtained at the beginning of the run, the P pressure is continuously matched to the Ar pressure. (Although the P pressure is adjusted by changing the heater power and therefore the reservoir temperature, note that the variable controlled by the controller feedback loop is the differential pressure, rather than the temperature.) After the Ar pressure has been raised to the desired value, and sufficient time has elapsed for the melt to become saturated with P, the boat temperature is slowly reduced, causing the melt to solidify gradually beginning at the colder end of the boat (the right end in Figure 3-1). After solidification is complete, the system is cooled and the Ar and P pressures are reduced.

Ten runs have been made in the pressure-balanced system to date. Although seeding has not yet been achieved, the ingots have very large grains. In one run, the In charge was doped with 0.1-at.% Fe. Over a period of 14 h during solidification, the P pressure was controlled at 25.17 atm with a variation of only $\pm$ 0.03 atm. The ingot obtained was semi-insulating and contained untwinned grains over 1 cm on a side.

All of the other ingots have been nominally undoped. The P pressures have ranged from 15 to 35 atm, corresponding to melt compositions from 45- to > 50-at.% P. Values of the measured carrier concentrations range from low-10^{15} to mid-10^{16} cm^{-3}. The data are scattered, but in general material grown under higher pressure exhibits higher carrier concentrations. Chemical analysis is planned to determine whether the donors in ingots with higher concentrations are Si. If so, experiments will be carried out to determine whether the Si originated from the silica boat or ampoule or from the starting In or P. If the silica is the source, the use of a pyrolytic BN boat or a BN coating on the inside of the ampoule may prevent the contamination. If the donors are not Si, they may be native defects. In any case, the trend of increasing carrier concentration with increasing P content of the melt is consistent with results that we have obtained for LEC crystals, in which the residual carrier concentration is reduced by growth from In-rich melts [2].

G.W. Iseler
H.R. Clark, Jr.

3.2 HYDROGEN ANNEALING OF PtSi-Si SCHOTTKY-BARRIER CONTACTS

Silicide-Si Schottky-barrier contacts are essential elements of current Si device and integrated circuit technology [3]. In particular, PtSi-Si Schottky-barrier contacts are extensively utilized because their barrier heights are favorable for many device applications. Contacts between PtSi and *n*-type Si, which have relatively high barrier heights ($\phi_{Bn} > 0.8$ eV), are widely used in bipolar integrated circuits.

Contacts between PtSi and *p*-type Si, which have low barrier heights ($\phi_{Bp} < 0.25$ eV), are used in fabricating infrared detectors [4] for the 3- to 5-μm spectral band.

In developing PtSi-Si detectors, we have observed that the values of ϕ_{Bp} are consistently reduced by 10 to 15 meV by H_2 annealing at 250 to 400°C. To gain an understanding of the mechanism of barrier-height reduction, we have fabricated PtSi-Si Schottky-barrier diodes on both *p*- and *n*-type Si substrates and determined their barrier heights before and after annealing in H_2 and in vacuum. The results can be explained by the presence of Si interface defects that are passivated by hydrogen incorporation and reactivated by vacuum annealing to remove the hydrogen.

The substrates used were 3-in-diam. Czochralski-grown (100) Si wafers doped either *p*-type with B to 20- to 40-Ω cm resistivity or *n*-type with P to 1- to 10-Ω cm resistivity. The Schottky-barrier diode structure is similar to that of the silicide infrared detectors described earlier [5], except that the test diodes have a back-side contact. Formation of the PtSi film was carried out by electron-beam deposition and subsequent in situ annealing of a Pt film 1 to 2 nm thick in an ultrahigh-vacuum (UHV) system. After diode fabrication, a number of the devices were annealed in flowing H_2 in a tube furnace and/or at a pressure of about 10^{-7} Torr in a separate vacuum system. Each of the post-fabrication annealing steps was carried out for 30 min at 300°C.

Forward current-voltage (I-V) curves have been measured at liquid nitrogen temperature to determine ϕ_B for Schottky-barrier diodes fabricated on many *p*-type substrates and on several *n*-type substrates. The variation in ϕ_B is typically no more than 2 meV for devices on a single substrate. For diodes on *p*-type substrates, which we shall refer to as *p*-type devices, the as-fabricated values of ϕ_{Bp} have ranged from 0.195 to 0.198 eV. The effects of H_2 annealing are illustrated by Figures 3-4(a) and (b), which show forward I-V curves for two pairs of typical Schottky-barrier diodes that were fabricated on a *p*-type substrate and on an *n*-type substrate, respectively. One device of each pair was annealed in H_2. This process decreased ϕ_{Bp} from 0.197 to 0.184 eV and increased ϕ_{Bn} from 0.914 to 0.927 eV. The changes in ϕ_B are thus equal in magnitude but opposite in sign. In every case, annealing produced a change of 10 to 15 meV in ϕ_B from the as-fabricated value, a decrease in ϕ_{Bp} and an increase in ϕ_{Bn}. The value of 0.184 eV for ϕ_{Bp} after H_2 annealing is less than the lowest previously reported value [6] for PtSi-Si diodes on *p*-type substrates, 0.187 eV.

Additional annealing experiments showed the effects of H_2 annealing to be reversible. Figure 3-5 shows the changes in ϕ_{Bp} observed in such experiments on the as-fabricated and H_2-annealed *p*-type diodes of Figure 3-4(a). Both devices were vacuum annealed, then H_2 annealed, and then vacuum annealed again. For both devices, the first vacuum anneal increased ϕ_{Bp} to 0.198 eV. The H_2 anneal then decreased ϕ_{Bp} to 0.190 eV, and the second vacuum anneal again increased ϕ_{Bp}, this time to 0.202 eV. For the *n*-type diodes of Figure 3-4(b), only one vacuum anneal was performed. In this case, the value of ϕ_{Bn} for the as-fabricated device did not change significantly, while the value of ϕ_{Bn} for the H_2-annealed device decreased to the as-fabricated value.

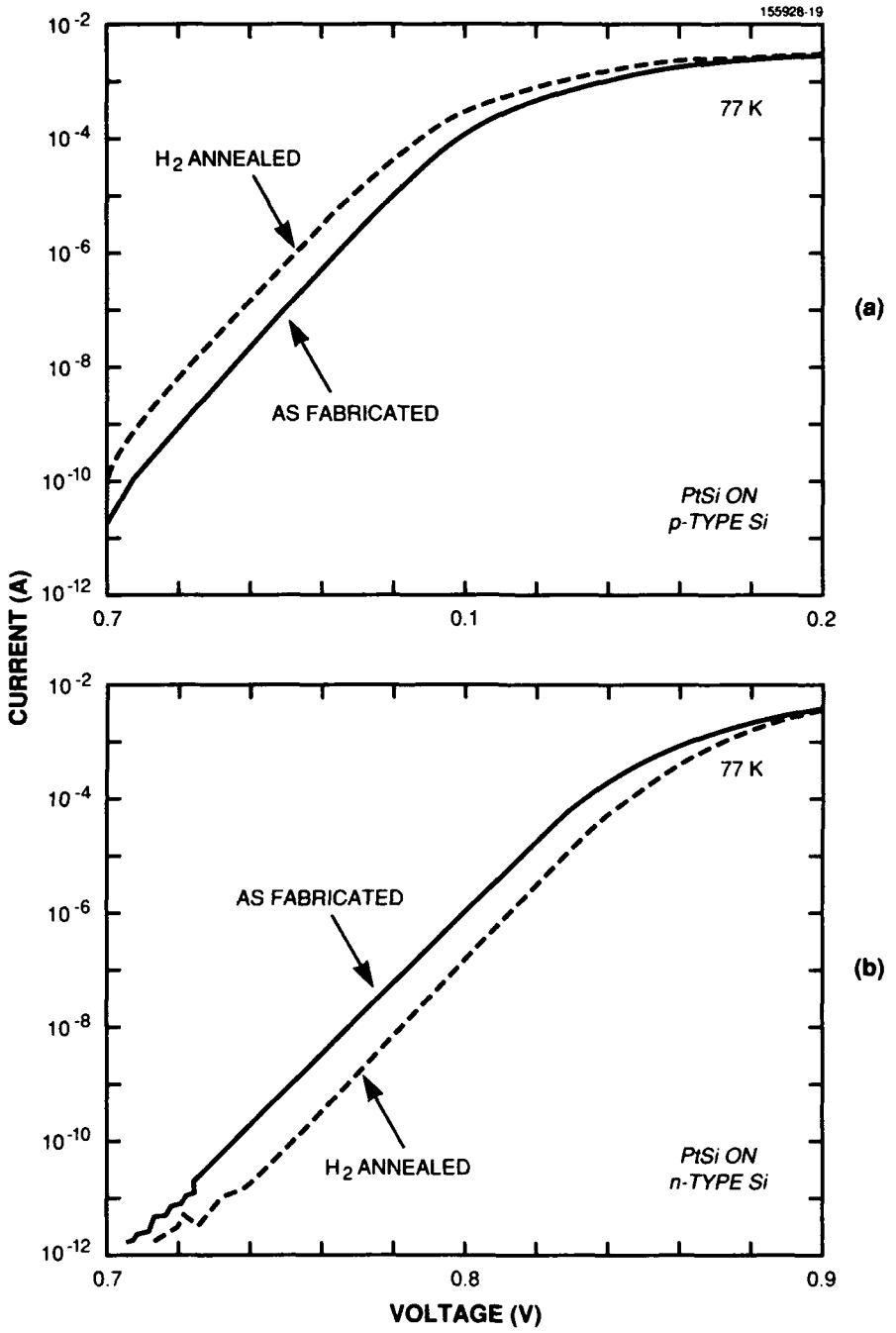

Figure 3-4. Forward I-V characteristics at liquid nitrogen temperature for as-fabricated and H_2-annealed PtSi-Si Schottky-barrier diodes fabricated on (a) p-type and (b) n-type Si substrates. H_2 annealing decreases the barrier height of p-type devices and increases the barrier height of n-type devices.

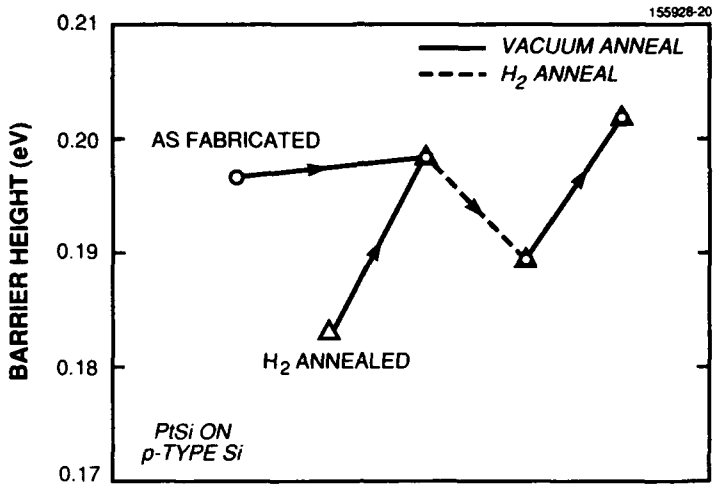

Figure 3-5. Barrier heights of p-type devices after successive H_2 and vacuum annealing.

To account for the annealing results, we propose a qualitative explanation based on a defect model that has been employed [7],[8] in analyzing the electronegativity dependence of the values of ϕ_{Bn} for metal and metal silicide contacts to *n*-type Si. According to this model, electrically active defects having energy levels lying within the Si bandgap can be present in the Si substrate close to the metal-Si or silicide-Si interface. For metals and silicides with sufficiently high electronegativities, such as PtSi, these interface levels are almost all unoccupied, and their positive charge produces a fixed electric dipole whose magnitude depends on their concentration. This concentration can be high enough to produce a significant decrease in the Si band bending at the interface and a corresponding decrease in ϕ_{Bn} with respect to the defect-free value. Schematic space-charge and energy-level diagram for an as-fabricated *n*-type PtSi-Si diode containing such midgap interface defects are shown at the left side of Figure 3-6; the corresponding diagrams for the device after H_2 annealing are shown at the right side. The dipole due to the charged defects lying above the Fermi level is represented in the space-charge diagrams by the open arrow on the Si side of the interface and the solid arrow of the same length on the PtSi side. This dipole has the same polarity as the dipole due to the Si space-charge region, which is represented in the diagrams by the positive charges on the Si side and the longer solid arrow on the PtSi side. We propose that annealing the diode in H_2 results in the diffusion of hydrogen through the thin PtSi film into the Si, where it passivates some of the interface defects. (Such H_2 passivation of interface states is a well-known phenomenon in Si metal-oxide-semiconductor technology [9].) The resulting decrease in the defect-induced dipole requires an increase in the space-charge-induced dipole in order to maintain the alignment of the Fermi levels in the PtSi and Si. This increase is accomplished by widening the space-charge region, which causes an increase in the Si band bending and therefore in the value of ϕ_{Bn}. Subsequent vacuum annealing removes the hydrogen, thereby reactivating the defects and restoring the as-fabricated properties.

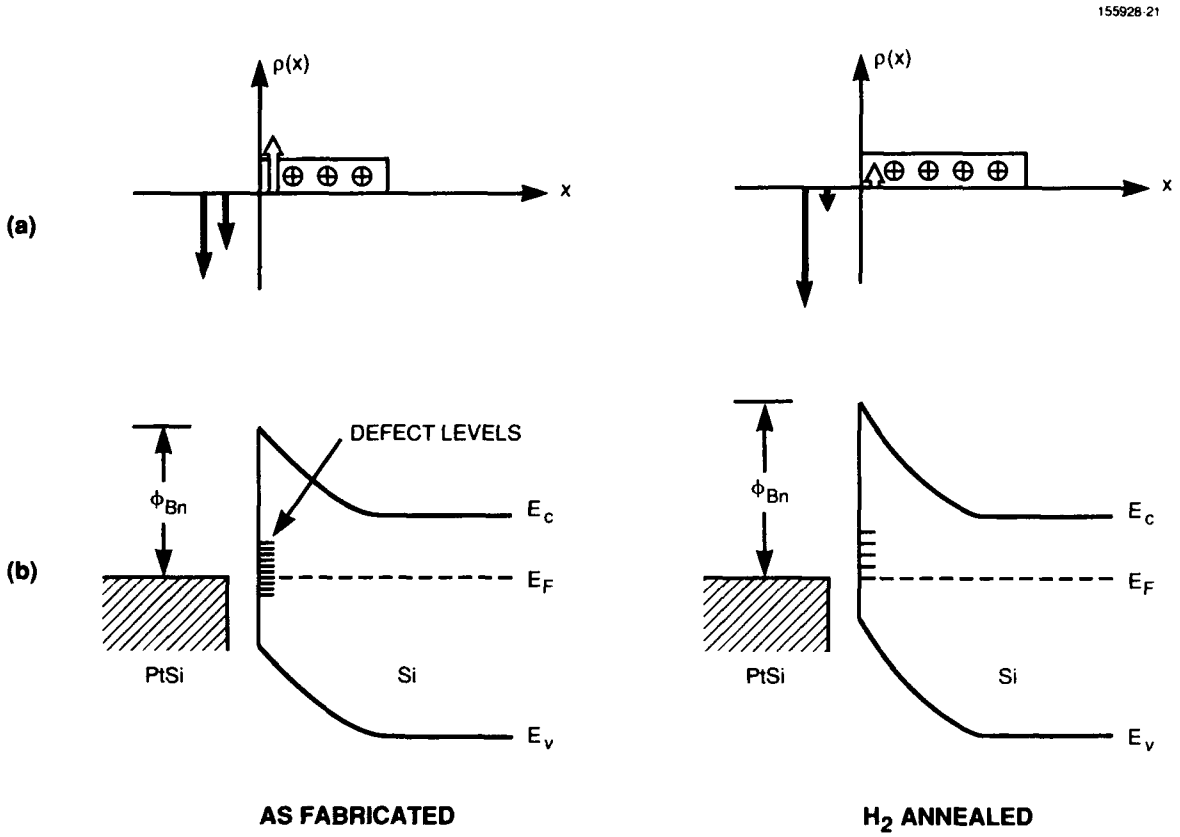

Figure 3-6. Schematic (a) space-charge and (b) energy-level diagrams for as-fabricated and H_2-annealed PtSi-Si Schottky-barrier diodes on n-type Si substrates. $\rho(x)$ represents the space-charge density.

The interface defects that influence the barrier heights of metal and metal silicide contacts to *n*-type Si have not been positively identified, although a Si-vacancy, dangling-bond model has been proposed [10]. In any case, there is evidence that at least some of these defects are introduced during contact formation. The processing procedure must also affect the ϕ_{Bn} value for PtSi-Si diodes on *n*-type Si substrates, since the value measured at room temperature for our as-fabricated devices is 0.90 eV, which significantly exceeds the highest value previously reported [11], about 0.87 eV. We believe that the use of a UHV system for Pt deposition and annealing has been largely responsible for the increase in ϕ_{Bn} for our as-fabricated diodes.

Neither the general electronegativity dependence of the values of ϕ_{Bp} for metal and metal silicide contacts to *p*-type Si nor the specific influence of interface defects on these values has been discussed in the literature. However, defects of the same kind can be expected to cause opposite changes in ϕ_{Bp} and ϕ_{Bn}, and a given processing procedure can be expected to yield the same kind and density of defects for

substrates of both types. Our observation that equal but opposite changes in ϕ_{Bp} and ϕ_{Bn} are produced by H_2 annealing is consistent with these expectations, as is the observation that the change in ϕ_{Bp}, like that in ϕ_{Bn}, is reversed by vacuum annealing.

B-Y. Tsaur
J.P. Mattia
C.K. Chen

REFERENCES

1. E.M. Monberg, W.A. Gault, F. Dominguez, and F. Simchock, *J. Electrochem. Soc.* **135**, 500 (1988).
2. G.W. Iseler, *J. Electron. Mater.* **13**, 989 (1984).
3. See, for example, K.N. Tu and J.W. Mayer, in *Thin Films Interdiffusion and Reactions*, J.M. Poate, K.N. Tu, and J.W. Mayer, eds. (Wiley, New York, 1978), p. 359.
4. F.D. Shepherd, *Int. Electron Devices Mtg. Tech. Dig.* (IEEE, New York, 1984), p. 370.
5. B Y. Tsaur, M.M. Weeks, and P.W. Pellegrini, *IEEE Electron Device Lett.* **9**, 100 (1988).
6. M.M. Weeks and P.W. Pellegrini, *Proc. SPIE* **1108**, 31 (1989).
7. P.E. Schmid, *Helv. Phys. Acta* **58**, 371 (1985).
8. W. Mönch, *Phys. Rev. Lett.* **58**, 1260 (1987).
9. B.E. Deal, *IEEE Trans. Electron Devices* **ED-27**, 606 (1980).
10. O.F. Sankey, R.E. Allen, and J.D. Dow, *Solid State Commun.* **49**, 1 (1984).
11. R. Purtell, G. Hollinger, G.W. Rubloff, and P.S. Ho, *J. Vac. Sci. Technol. A* **1**, 566 (1983).

4. SUBMICROMETER TECHNOLOGY

4.1 POLYSILYNE THIN FILMS AS RESISTS FOR DEEP-UV LITHOGRAPHY

The application of a new class of Si-containing polymers as UV photoresists is reported. The first synthesis of this class of Si-Si backbone polymers, the polysilynes ($[SiR]_n$), was reported in 1988 [1]. Unlike the linear polysilanes, these polymers contain only one pendant alkyl group per silicon atom. Their structure, however, bears no similarity to polyacetylene, their carbon-backbone analog. Rather, polysilyne molecules exist as Si-Si *s*-bonded networks [2] and exhibit photochemical and dry etch properties that make them attractive as both wet- and dry-developed resists in UV-based bilayer lithography.

The polysilynes $[SiR]_n$ studied were R = *n*-butyl, isobutyl, amyl, cyclohexyl, and phenyl. Following purification, the polysilyne polymers were isolated as yellow, moderately air- and light-sensitive powders with mean molecular weights ranging from 8,000 to 100,000 daltons, or approximately 300 to 1,000 alkylsilicon units. When protected from light and air the polysilynes remained freely soluble in nonpolar organic solvents. Once in solution, the samples were passed through a 0.2-μm filter and spin coated onto various substrates using either toluene, xylene, or trichloroethane as the solvent.

The most notable change upon polysilyne photolysis is the conversion of the Si-Si network into a predominantly Si-O network, accompanied by a significant reduction in UV absorption. Figure 4-1 illustrates the effect of 193-nm exposure on the UV spectrum, when the films were exposed in air. The film thicknesses were approximately 40 nm. The spectra of poly(*n*-butylsilyne) in Figure 4-1(a) show significant bleaching down to 190 nm, whereas the poly(phenylsilyne) [Figure 4-1(b)] remains absorptive at wavelengths less than 230 nm, presumably because of the aryl functionality. The other alkyl-substituted silynes such as isobutyl, amyl, and cyclohexyl exhibit behavior similar to that of *n*-butyl shown in Figure 4-1(a). Fourier-transform infrared spectroscopy and *x*-ray photoelectron spectroscopy have shown that the oxidized polysilyne is a siloxane, whereas Auger electron spectroscopy indicates a marked increase in oxygen content. For instance, the silicon-to-oxygen ratio of poly(*n*-butylsilyne) exposed to a dose of 100 mJ/cm^2, at a fluence of 0.1 mJ/cm^2 per pulse, increased from 1:0.6 to 1:1.2.

The solubility of a polysilyne in nonpolar organic solvents is greatly reduced upon oxidation. This reduction in solubility allows for selective development of unexposed polymer. In general, a dose of 50 to 200 mJ/cm^2 at 193 nm is necessary to render thin polysilyne films insoluble in toluene, xylene or trichloroethane. Figure 4-2 shows the remaining (insoluble) polysilyne thickness after exposure at 193 nm and development in toluene. The slopes and intercepts of the curves corresponding to different polysilynes differ from each other. It is therefore clear that the R group affects the dissolution of the exposed material. This may be a result of differences in molecular weight, as the large R-group polymers are usually lower in molecular weight and exhibit generally higher solubility.

In addition to the wet-development studies, the dry-etch selectivity between photooxidized and unirradiated polysilyne surfaces was examined using an RF-powered, parallel-plate reactive ion etcher (RIE). The etch chemistries investigated were for Cl_2 and BCl_3. Both aryl- and alkyl-substituted polysilynes exhibited dry-etch selectivity after laser exposure, with the laser-oxidized surface exhibiting in-

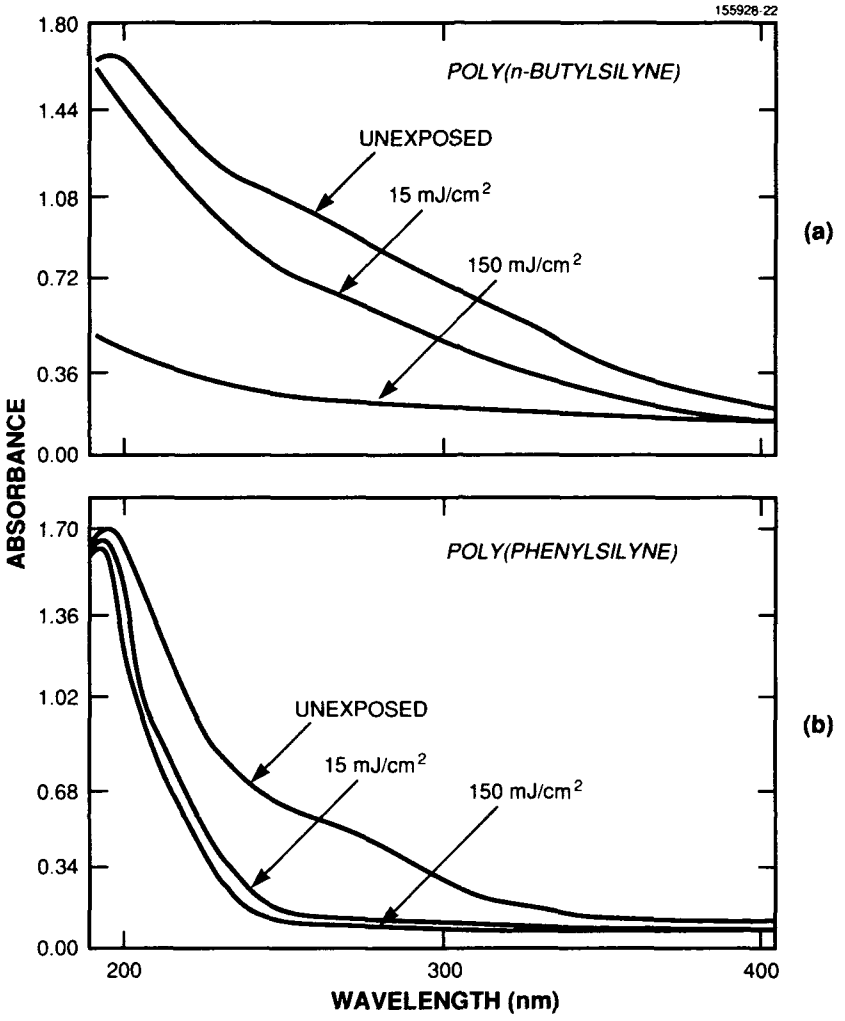

Figure 4-1. (a) UV absorption spectra for poly(n-butylsilyne) unexposed, exposed to 15 mJ/cm^2 at 193 nm, and exposed to 150 mJ/cm^2 at 193 nm. (b) Same as (a), but for poly(phenylsilyne). The film thicknesses were approximately 60 nm.

creased etch resistance (negative tone). Typical unexposed-to-exposed etch selectivities were between 1:1 and 3:1 for the poly(alkylsilynes) and as high as 15:1 for poly(phenylsilyne). At bias voltages greater than –200 V, there was very little etch selectivity for any of the polysilynes. The minimum dose necessary to effect an increase in the dry-etch resistance was typically two times higher than that necessary to induce insolubility in toluene. We note that the selectivities reported here should be further increased through the use of high-flux, low-bias etching techniques such as magnetron- or electron-cyclotron-resonance RIE. Both the exposed and unexposed polysilynes are very resistant to oxygen RIE. For example, all the polysilynes exhibit etch selectivities of roughly 50:1 over hard-baked AZ photoresist for O_2 RIE at –150-V bias.

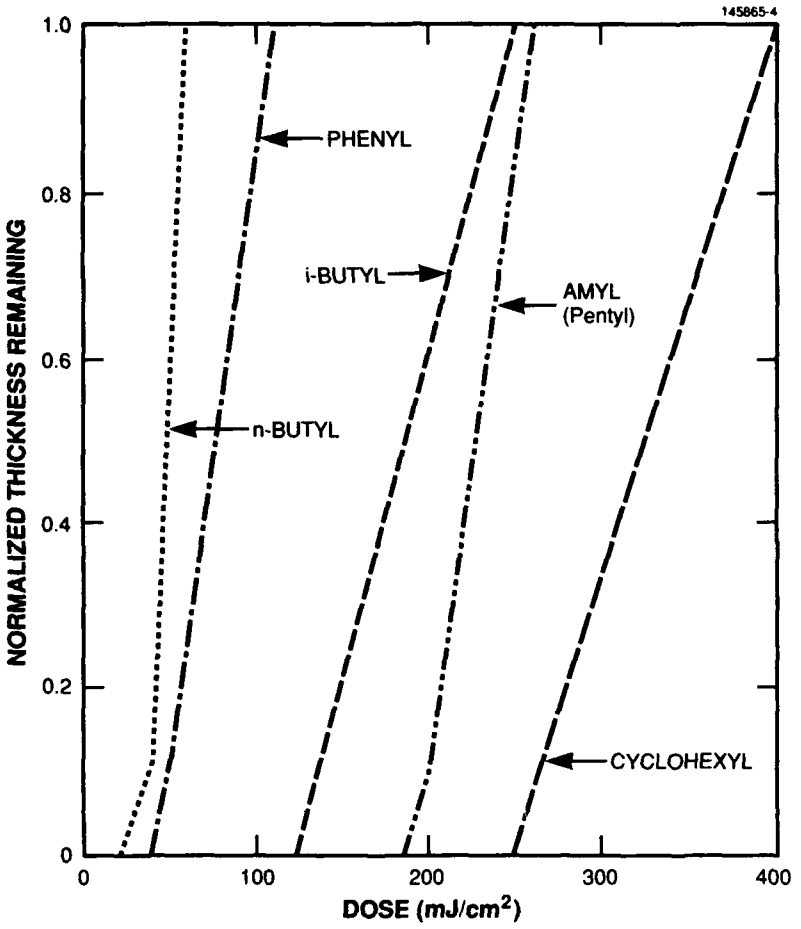

Figure 4-2. Dissolution curves for various polysilynes exposed at 193 nm at a fluence of 0.3 mJ/cm^2 per pulse and developed in toluene for 5 s. Film thicknesses were from 50 to 90 nm.

Patterning of the polysilynes was performed on our small-field 193-nm stepper. Based on contrast and sidewall uniformity, the best results with wet development were for poly(*n*-butylsilyne) using toluene as the developer (5 s at 22°C), followed by pattern transfer using O_2 RIE at –100-V bias. The results shown in Figures 4-3 (a) and (b) for 0.37-μm and 0.45-μm lines and spaces, respectively, were obtained with an exposure of 125 mJ/cm^2 at 1 mJ/cm^2 per pulse. The resist thickness was 50 nm, and the substrate was 1 μm of PMMA. For selective dry development, only the poly(phenylsilyne) has thus far offered good results. The RIE development was in Cl_2 plasma with 100-mTorr pressure at 50-W power with the bias at –50 V, followed by O_2 RIE at –150-V bias. These results, shown in Figures 4-4(a) and (b) for 0.40-μm and 0.75-μm lines and spaces, respectively, were obtained with an exposure of 330 mJ/cm^2 at 0.3 mJ/cm^2 per pulse.

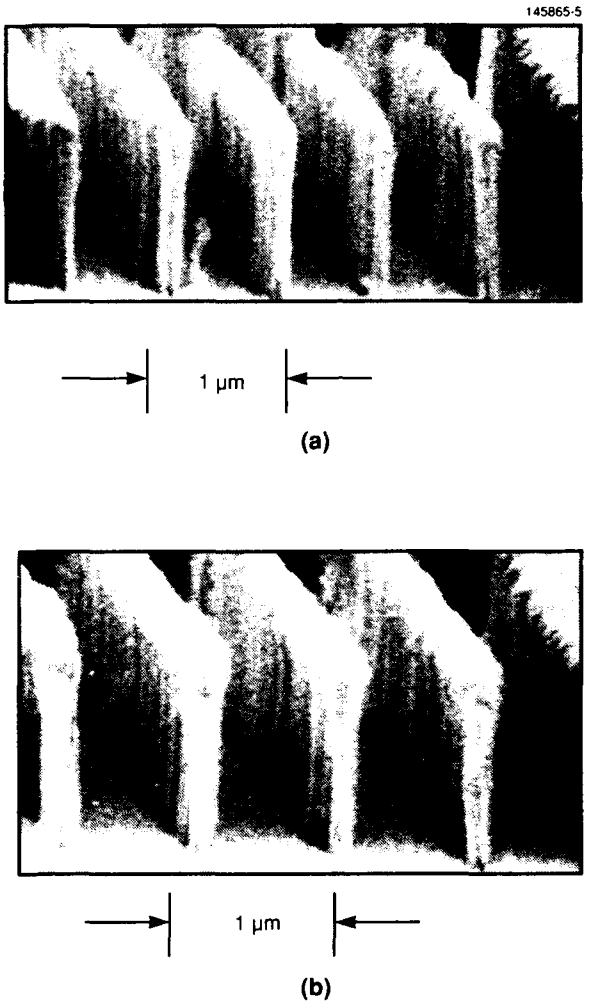

Figure 4-3. (a) 0.37-μm lines and spaces imaged in poly(n-butylsilyne), wet developed (negative tone) in toluene, and transferred through PMMA using O_2 RIE at −100 V bias. Exposure was 125 mJ/cm² at 1 mJ/cm² per pulse. (b) Same as (a), but 0.45-μm lines and spaces.

The efficient photooxidation of the polysilynes allows for a combination of selective development techniques for pattern definition. Features less than 0.4 μm were imaged, resulting in structures whose aspect ratios were greater than 3:1 after pattern transfer. At low doses (50 to 200 mJ/cm^2), polysilyne films become transparent in the UV and totally insoluble in many solvents, and act as negative tone resists. The resulting siloxane can be selectively dry developed in Cl_2 plasmas. In this dose regime, the

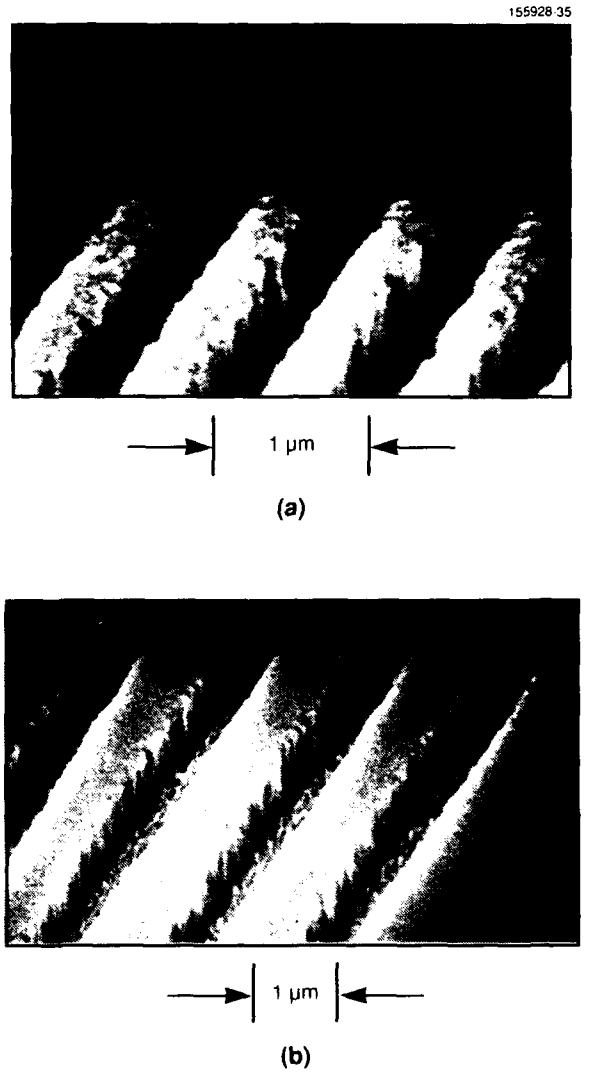

Figure 4-4. (a) 0.4-μm lines and spaces imaged in poly(phenylsilyne), dry developed (negative tone) in Cl_2 plasma at 100-mTorr pressure, 50-W power and –50-V bias, and transferred using O_2 RIE at –150-V bias. Exposure was 330 mJ/cm^2 at 0.3 mJ/cm^2 per pulse. (b) Same as (a), but 0.75-μm lines and spaces.

sensitivity of the polysilynes compares well with other 193-nm resists under investigation, such as those based upon selective silylation [3].

R.R. Kunz
M.W. Horn
P.A. Bianconi*
D.A. Smith*
C.A. Freed*

*Author not at Lincoln Laboratory.

4.2 WAFER-SCALE MASS MEMORY

Ever increasing amounts of memory are required in computer systems to support user-friendly interfaces, graphics, high-level languages, and databases. Several different types of memory subsystems are used to optimize the cost/performance ratio of the computer. Main memory provides high-speed data storage and is implemented using solid state dynamic random-access memory (DRAM) chips. Mass storage devices, typically magnetic disks, provide high-capacity storage at low cost, but often impose substantial performance limitations on the computer system.

We have used wafer-scale integration techniques to fabricate a low-cost, high-speed mass memory module based on solid state DRAM technology. This module uses commercial DRAM wafers with the addition of a low-resolution, low-cost interconnect fabricated on the wafer. A memory system based on this module would be at least three orders of magnitude faster than disk memory, would be substantially less expensive than main memory, and would benefit from future improvements in density and cost for DRAM technology.

Wafer-scale integration applications have been restricted by power dissipation and fault tolerance limitations. In a memory system, power dissipation is manageable since only a small fraction of the memory cells are accessed at any one time. The regular architecture of a memory system facilitates fault-tolerant design. Redundant buses can be used to improve interconnect yield, and address-mapping techniques can be used to replace faulty memories with functional ones. The memory can be easily retested and remapped to repair field failures.

The wafer-scale memory architecture requires two levels of metallization to route the chip selects, address lines, data lines, and power connections. The fault tolerance of the design is enhanced through the use of conservative design rules and redundant bond pads and buses. The signal lines are routed on 20-μm-wide metal conductors set on a 100-μm pitch with 24-μm-wide vias. Connections to the chip bond pads use 80-μm-wide vias. Power is routed on 3.6-mm-wide buses. Most of the long buses are routed on the top level of metal to reduce the wiring capacitance. Pads located at the perimeter of the wafer are used to connect the wafer-scale memory to a printed circuit board. The pads are designed to accept conventional wire bonds or a pressure-type connector.

We have developed a simple fabrication sequence for constructing the wafer-scale memory, starting with 125-mm-diam. DRAM wafers. The wafers contain 195 memory chips each comprising one million bits. On any given wafer, approximately 50 percent of the chips are perfect and the remaining chips contain substantial numbers of good bits. Address-mapping techniques permit the use of the partially functional chips and should increase the effective yield to 90 percent, which would give 22 Mbytes of storage per wafer. Figure 4-5 illustrates a cross section of the interconnect fabricated on the wafers. Although the wafers have been passivated, the manufacturer's metallization may contain hillocks that puncture the passivation layer. To prevent shorts to the wafer-scale interconnect, an additional dielectric layer is fabricated prior to metallization. A 3-μm-thick layer of MP 1400-37 photoresist is used as a photosensitive dielectric layer to simplify the processing. The use of a thick dielectric layer planarizes the surface to improve the continuity of the metallization. The vias are patterned in a proximity printer, and the exposure and development conditions are controlled to produce a sloped-sidewall via, which

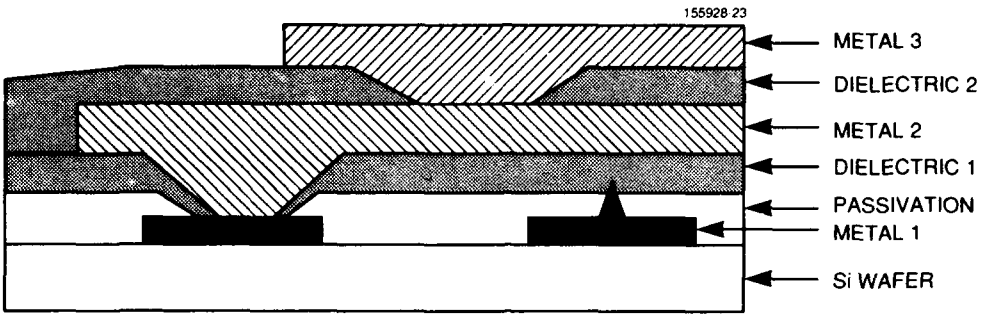

Figure 4-5. Cross section of wafer-scale memory interconnect. Layers designated dielectric 1, metal 2, dielectric 2, and metal 3 were fabricated at Lincoln Laboratory on the commercial DRAM wafers.

ensures good metal coverage. After patterning, the photoresist is baked at 160°C for 1 h, making the film impervious to further processing. Both metal layers are 1-μm-thick electron-beam-evaporated aluminum. The metallization is patterned using a contact printer and wet etch.

The first completed wafer-scale memory module is shown in Figure 4-6. Extensive optical examination of the wafer has revealed a number of defects in the interconnect. In the first metallization the aluminum etchant apparently undercut the patterning resist reducing the overall quality of the metal and introducing several breaks. There were three shorts in the second metal busing, but these can be repaired using laser-cutting techniques. In several areas the dielectric and metallization appeared to have been damaged by particles during the contact lithography. Despite these defects, the redundant-bus architecture assures that substantial portions of the wafer-scale memory will be operational. Improved cleanliness and the use of projection lithography would improve the yield on future systems.

The use of photoresist as a dielectric simplifies the wafer processing, but has led to several problems. Early experiments indicated that the dielectric would crack in the vicinity of vias if the vias were misaligned. Revising the design rules to increase the amount of metal surrounding the vias remedied this problem. Forming low-resistance contacts has also presented a difficulty, since the aluminum conductors oxidize during processing, forming an insulating film between the metal layers. For the prototype wafer-scale module, we used a mild wet etchant to remove the oxide, followed immediately by the evaporation of the aluminum layer. The contacts initially exhibited 100-kΩ impedance, but would break down at less than 1 V. Following breakdown, the contact resistance is permanently reduced to less than 10 Ω. For the prototype module this behavior is acceptable, but further improvements are under study. While a post-deposition sinter could be used to improve the contacts, this would overheat the photoresist dielectric. Sputter-deposited aluminum with in situ cleaning is usually used to form good contacts, but this step also heats the substrate. Currently, high-temperature photoresists compatible with such heating are being investigated.

T.M. Lyszczarz
D.C. Shaver
J.I. Raffel

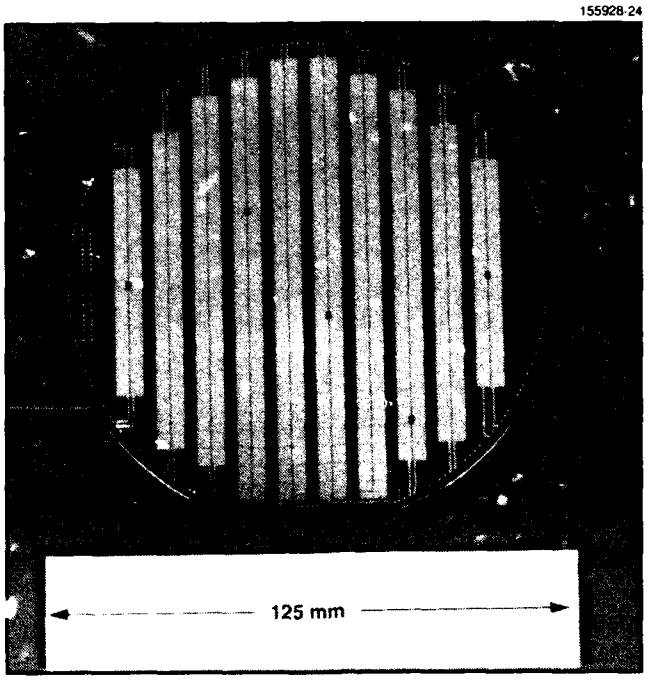

Figure 4-6. Photograph of completed wafer-scale memory module. The input/output pads are clearly visible at the perimeter of the wafer. Power and ground buses run vertically across the wafer.

REFERENCES

1. P.A. Bianconi and T.W. Weidman, *J. Am. Chem. Soc.* **110**, 2342 (1988).

2. P.A. Bianconi, F.C. Schilling, and T.W. Weidman, *Macromolecules* **22**, 1697 (1989).

3. M.A. Hartney, R.R. Kunz, D.J. Ehrlich, and D.C. Shaver, to be published in *J. Vac. Sci. Technol. B* **7** (1990).

5. MICROELECTONICS

5.1 SUBMILLIMETER-WAVE OSCILLATIONS IN InAs/AlSb RESONANT-TUNNELING DIODES

The resonant-tunneling diode (RTD) is one of the most promising devices to fill the need for solid state oscillators operating in the submillimeter-wave band between 300 and 1000 GHz. For a 1.5-μm-diam. double-barrier RTD consisting of an InAs quantum well and AlSb barriers, we have recently achieved oscillation frequencies up to 675 GHz at a maximum CW power of ~ 0.5 μW and power density of ~ 25 μW cm^{-2}. The best previous result was a frequency of 420 GHz at a CW power of 0.2 μW and power density of 2 W cm^{-2}, obtained in a 4-μm-diam. GaAs/AlAs diode [1]. The 675-GHz result represents the highest known oscillation frequency for any solid state device.

The InAs/AlSb materials system has recently been implemented to make high-performance RTDs [2], for example, a diode having a peak current density J_P of 3.7×10^5 A cm^{-2} and a peak-to-valley ratio of 4:1 at room temperature. The curve of current density versus voltage for this device is given in Figure 5-1 in comparison with plots for the best high-current-density diodes from the other materials systems used for RTDs, GaAs/AlAs and $In_{0.53}$ $Ga_{0.47}$ As/AlAs. In the present report, we describe an InAs/AlSb diode having a slightly lower J_P of 2.8×10^5 A cm^{-2}, but the same peak-to-valley ratio as shown in Figure 5-1. All epitaxial layers in the diode are grown by molecular beam epitaxy at 500°C on a semi-insulating GaAs substrate. Two 1.5-nm-thick AlSb barriers are separated by a 6.4-nm-thick InAs quantum well. Adjacent to the double-barrier structure are lightly doped spacer layers that extend 20 and

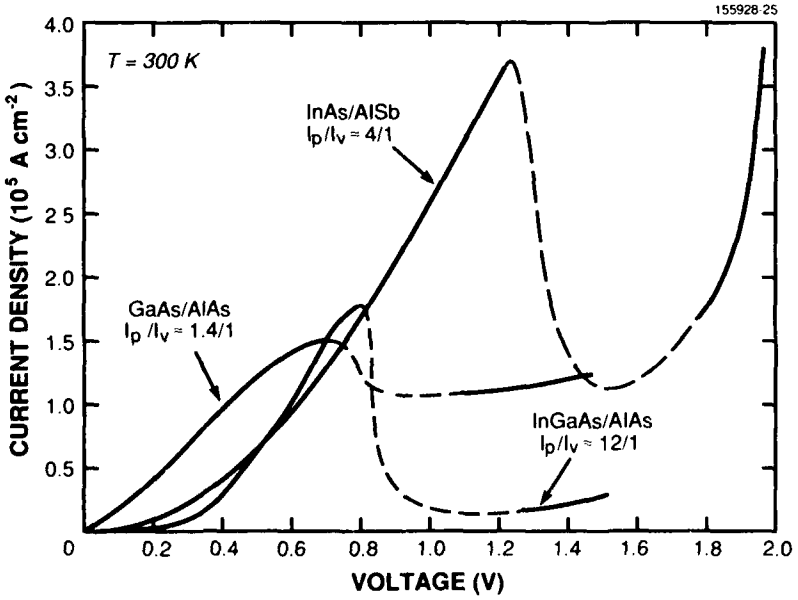

Figure 5-1. Room-temperature current density versus applied voltage of three materials systems used for RTDs.

75 nm beyond the cathode and anode sides, respectively. Outside of the spacer layers are 200-nm-thick n-type epitaxial layers doped to a concentration N_D of 2×10^{18} cm^{-3}, and outside of these layers are more heavily doped epitaxial layers that extend to the top ohmic contact and to a superlattice buffer layer.

Our experimental technique is to use the negative differential resistance region of the diode as the basis for oscillations in each of four waveguide resonators, covering the frequency range from 100 to 700 GHz. As in previous experiments, the maximum CW power is determined for each resonator, and the frequency corresponding to this power is measured with waveguide or quasi-optical wavemeters. Our results for a 1.5-μm-diam. diode are 20 μW at 110 GHz, 10 μW at 205 GHz, 3 μW at 360 GHz, and ~ 0.5 μW at 675 GHz. Preliminary indications are that the 675-GHz result is a fundamental rather than a harmonic of a lower-frequency oscillation, but further work is necessary on this important matter. The experimental results are shown in Figure 5-2 in comparison with the highest-frequency results obtained in diodes made from the other materials systems. The InAs/AlSb result at 360 GHz represents a power density of 160 W cm^{-2}, which is an 80-fold improvement over the best result for GaAs/AlAs diodes at approximately the same frequency. All of the InAs/AlSb power levels could be increased roughly tenfold in existing resonators by increasing the diameter of the diode to about 5 μm.

We attribute these excellent results to the high available current density, $J_P - J_V = 2.1 \times 10^5$ A cm^{-2}, and the very low series resistance of the present InAs/AlSb device. The low series resistance is due primarily to the nearly ideal ohmic contact that can be formed to InAs. The value of the specific contact

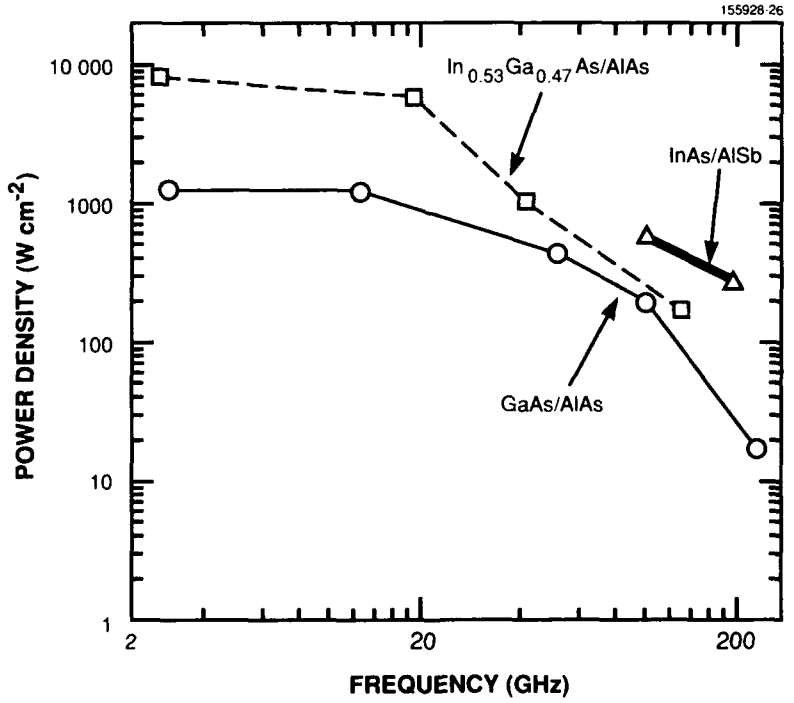

Figure 5-2. Oscillation results for the fastest RTDs made from three materials systems.

resistance is so low that it is difficult to measure, but from the oscillator results we estimate it to be about $1 \times 10^{-7}\ \Omega\ cm^2$. This leads to a theoretical value for the maximum oscillation frequency of at least 1.3 THz.

E.R. Brown
C.D. Parker
L.J. Mahoney

5.2 PROTON AND NEUTRON IRRADIATION OF CCD IMAGING DEVICES

Continuing the characterization of proton-irradiated silicon charge-coupled devices (CCDs) from our previous report [3], we have examined the effect of irradiation on bulk minority carrier diffusion length, dark current, and charge transfer efficiency (CTE). This work has allowed us to postulate a relationship between doping density and degradation of minority carrier lifetime and also to tentatively identify the phosphorus-vacancy (P-V) complex as the defect limiting CTE in irradiated phosphorus-doped material.

The minority carrier diffusion length of the samples was determined using the surface photovoltage technique. The post-irradiation diffusion length vs dopant concentration is shown in Figure 5-3. The figure indicates that the diffusion length for both P- and B-doped Si may be fit with an inverse 1/4 power

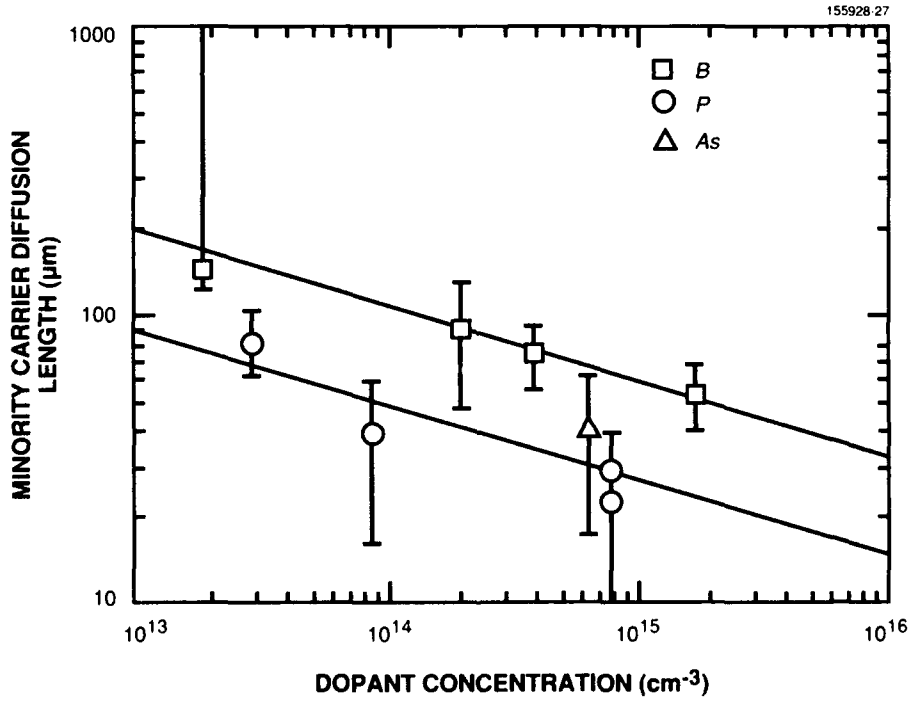

Figure 5-3. Diffusion length of bulk Si wafers after irradiation with 10 krad of 100-MeV protons. The effect of B, P, or As doping density on diffusion length is shown. The error bars refer to 95-percent confidence limits for each data point, and the straight line fits assume a 1/4 power dependence of diffusion length on dopant concentration.

dependence on dopant concentration. Since the number of defects that act as recombination centers is inversely proportional to the square of the diffusion length, such a fit implies that the number of defect sites is proportional to the square root of the doping density. If one assumes that microequilibrium exists between the defect sites and dopant density, then this square-root dependence suggests that bimolecular kinetics are involved and that two defects are generated at or near a dopant atom. It is also apparent from Figure 5-3 that the diffusion length of B-doped Si is superior to that of P-doped Si, suggesting that the channel of the CCD is more susceptible to damage than is the bulk.

We have not yet established a dependence of CTE or dark current on doping density, either in the buried channel or the underlying substrate, so we cannot say whether the decrease in minority carrier lifetime, increase of dark current, and decrease of CTE are related to the same defects in proton-irradiated Si. However, we have tentatively identified the deep-level P-V trap as limiting CTE. This has been done by measuring the trap emission time in irradiated CCDs, using a method described in Reference 4. Emission time constants are plotted vs the inverse temperature in Figure 5-4, along with the

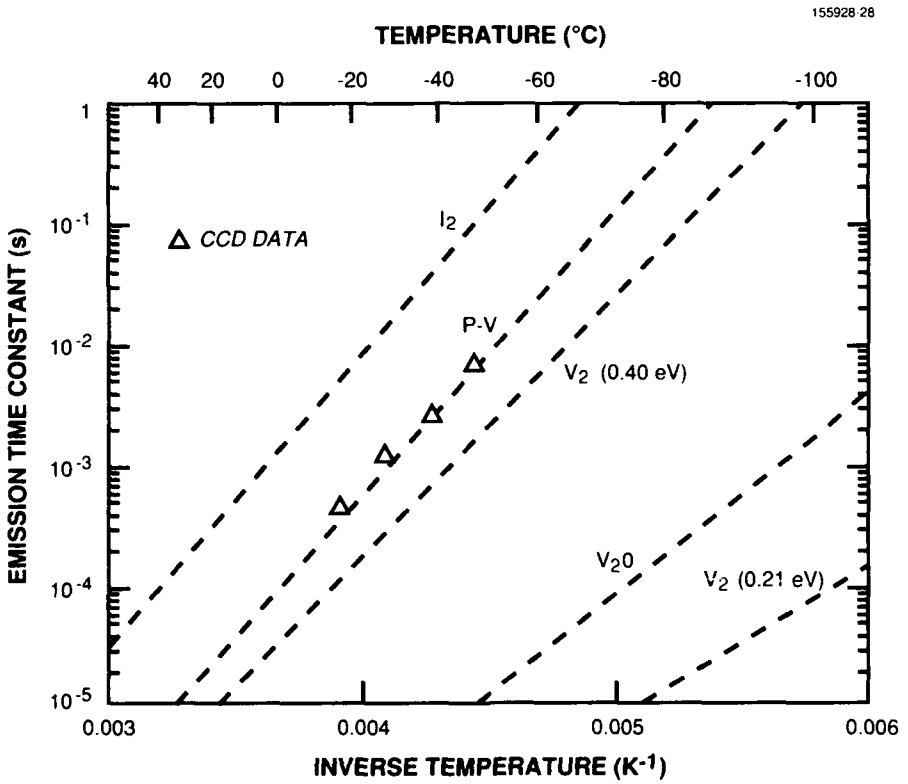

Figure 5-4. Emission time constants for proton-induced electron traps as a function of inverse operating temperature. The data points refer to measurements on a CCD irradiated with 2 krad of protons, while the dashed curves are the reported temperature dependence of emission times for specific defects in Si: tentatively identified silicon di-interstitial complex (I_2), phosphorus-vacancy complex (P-V), two distinct silicon divacancy complexes (V_2) labeled by trap depth, and tentatively identified silicon divacancy/oxygen interstitial complex (V_2O).

reported data on specific defects in Si [5]. It is apparent that there is good agreement between the data collected on proton-irradiated CCDs and the P-V defect in Si. One can also determine from Figure 5-4 an appropriate clocking frequency for operation of the CCD at a particular temperature; for clocking periods either long or short compared to the trap emission time, the CTE will suffer little degradation after irradiation. Indeed, this behavior is believed to be responsible for the apparent immunity of the serial register of the CCD reported in Reference 3. Traps in the serial register are filled by previous charge packets, and then succeeding charge packets are clocked fast enough that the captured charge cannot be reemitted before the new charge is clocked out.

Characterization of CCDs and test structures has also been carried out by neutron bombardment, and preliminary results suggest that the effects are roughly equivalent for the same dose of protons and neutrons.

J.A. Gregory
B.E. Burke
M.J. Cooper

REFERENCES

1. E.R. Brown, T.C.L.G. Sollner, C.D. Parker, W.D. Goodhue, and C.L. Chen, *Appl. Phys. Lett.* **55,** 1777 (1989).
2. J.R. Söderström, D.H. Chow, and T.C. McGill, *IEEE Electron Device Lett.* **11**, 27 (1990).
3. Solid State Research Report, Lincoln Laboratory, MIT (1989:4), p. 67.
4. A.M. Mohsen and M.F. Tompsett, *IEEE Trans. Electron Devices* **ED-21,** 701 (1974).
5. W. Wondrak, K. Bethge, and D. Silber, *J. Appl. Phys.* **62**, 3464 (1987).

6. ANALOG DEVICE TECHNOLOGY

6.1 SHALLOW-BURIED-CHANNEL CCDs WITH BUILT-IN DRIFT FIELDS

The performance of charge-coupled devices (CCDs) is limited by the charge that is left behind after the bulk of the charge packet has transferred by Coulomb repulsion. In the absence of drift fields these residual electrons will transfer by thermal diffusion, which is a very slow process. The CCD speed can be enhanced by designing structures with strong fringing fields between gates, such as deep-buried-channel CCDs. Deep-buried-channel delay lines have indeed been demonstrated at record speeds (hundreds of megahertz), but they have several disadvantages that may ultimately limit their usefulness. For example, the shape of the potential wells is distorted, degrading linearity and affecting the overall signal-processing performance of the CCD. Furthermore, the charge-handling capacity decreases as the channel moves into the bulk, and at least 10-V clocks are required. These 10-V clocks are not only difficult to generate at high speed, but are incompatible with the 5-V technology necessary for the high-performance on-chip support circuits that interface with the CCD.

To overcome these disadvantages we have designed, fabricated and tested shallow-buried-channel delay lines with a channel depth of 300 nm, which are operated with 5-V two-phase clocks and have a built-in potential gradient, generated by a step implant in the storage wells, to improve the charge transfer efficiency (CTE). We studied long-channel CCDs with storage gates 26 μm long, and short-channel CCDs with storage gates 7 μm long. In both cases the barrier electrodes are 4 μm long. The step-doped CCDs had to be designed with great care to ensure that the step doping was a small perturbation in the structure and did not, for example, make the wells so deep that they did not clear the following barrier, preventing complete transfer at any clocking rate. To estimate the effect of a small potential step ($\Delta V \approx 0.5$ V) we modeled the CCDs with CANDE, a two-dimensional device simulator.

Figure 6-1 shows the predicted channel potential for long-channel CCDs from which we derived the channel electric field. We then calculated the transit time for the uniform and step-doped devices to be 150 and 20 ns, respectively. The predicted channel potential for short-channel CCDs is shown in Figure 6-2. The corresponding transit time for the uniform and step-doped devices is 0.8 and 0.45 ns, respectively. Figures 6-1 and 6-2 confirm that the step is a small perturbation of CCD wells. From the simple calculation of the single-electron drift, which ignores diffusion, we cannot predict the improvement in the CTE or maximum clocking rate. Nevertheless, the calculations indicate that even a small potential step can result in a significant enhancement in the electron drift.

The devices tested are simple two-phase delay lines, which were designed so that the input, transfer and output clocking rates could be independently set. The CTE was measured in slow-input/fast-transfer/slow-readout experiments where the input and output clocking rates were too slow to affect the output signal. The CTE was generally constant up to a maximum clocking rate $f_{c(\max)}$, beyond which it degraded very rapidly. From $f_{c(\max)}$ we can then estimate the time T_t required for almost all of the electrons to transfer. For clock edges t_r and t_f,

$$f_{c(\max)} = \frac{1}{\left(2T_t + t_r + t_f\right)} \tag{6.1}$$

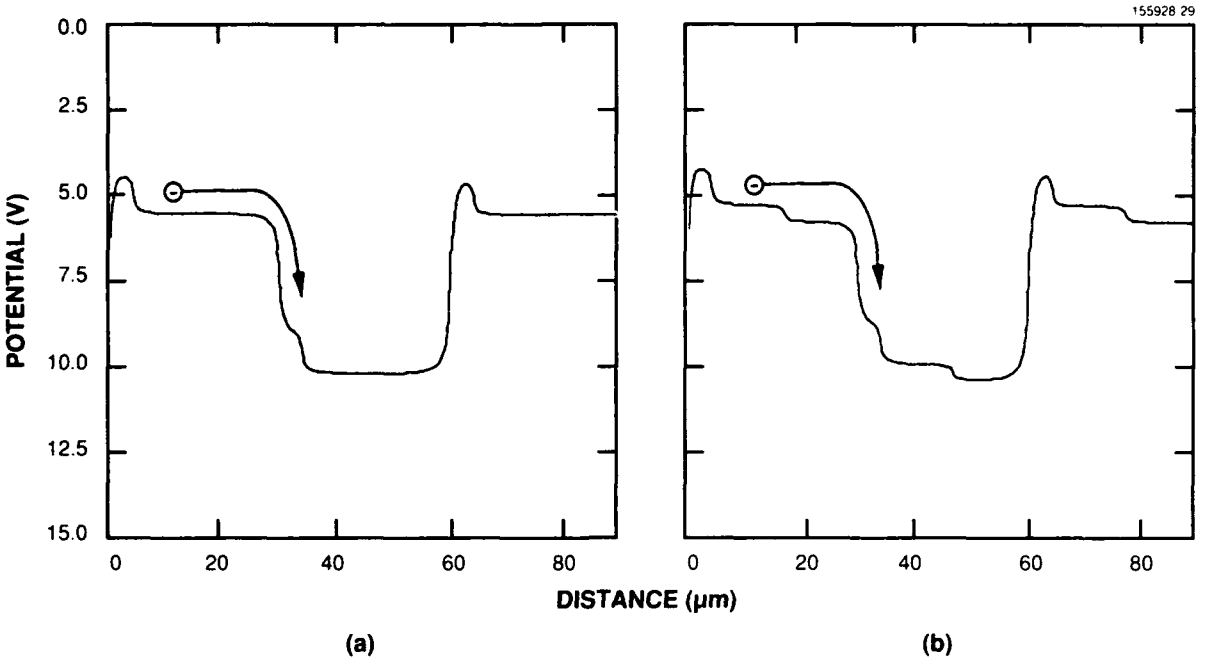

Figure 6-1. Channel potential calculated with CANDE for long-gate (L = 26 μm) (a) uniform and (b) step-doped CCDs.

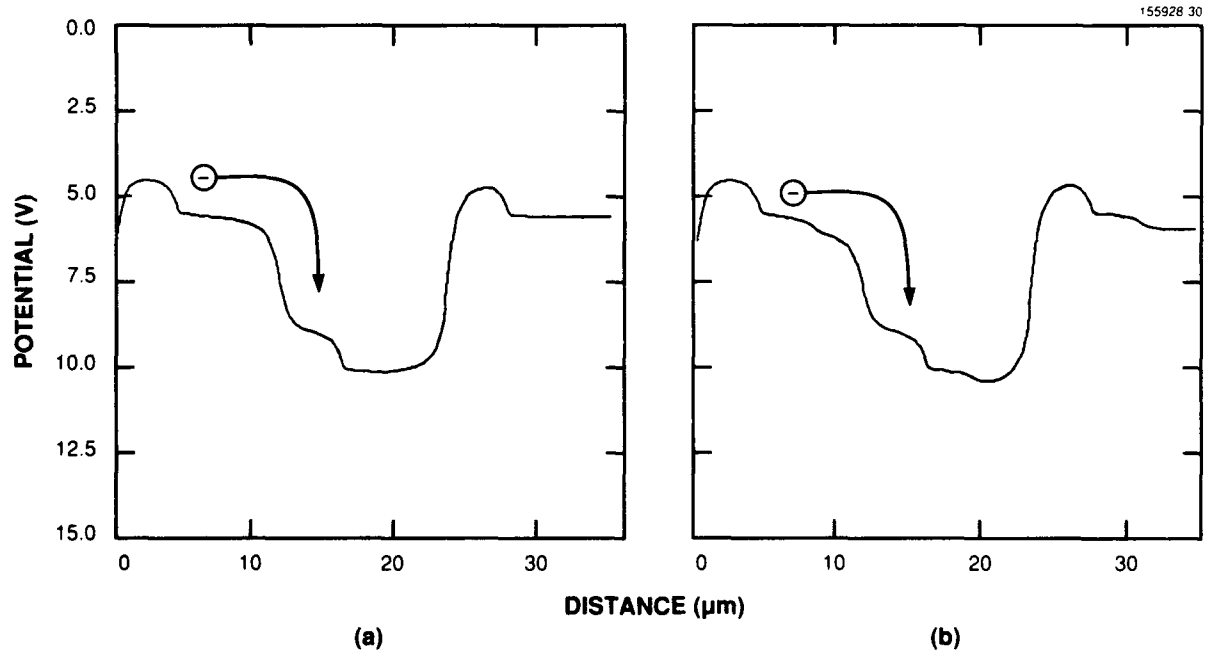

Figure 6-2. Channel potential calculated with CANDE for short-gate (L = 7 μm) (a) uniform and (b) step-doped CCDs.

or

$$T_t = \frac{1}{2}\left(\frac{1}{f_{c(\max)}} - t_r - t_f \right) . \tag{6.2}$$

For our experimental conditions $t_r \approx t_f \approx 1$ ns.

In the uniform long-channel CCDs, the CTE for low clocking rates is 0.9994 and for $f_c > 2.5$ MHz it degrades very rapidly. In the step-doped long-channel CCDs, the transfer loss is too small to measure (CTE > 0.99995) up to 12.5 MHz, beyond which it increases very rapidly. The transfer times corresponding to $f_{c(\max)}$ of 2.5 and 12.5 MHz are 200 and 40 ns, respectively. The outputs from both devices at 2.5 and 12.5 MHz are shown in Figure 6-3.

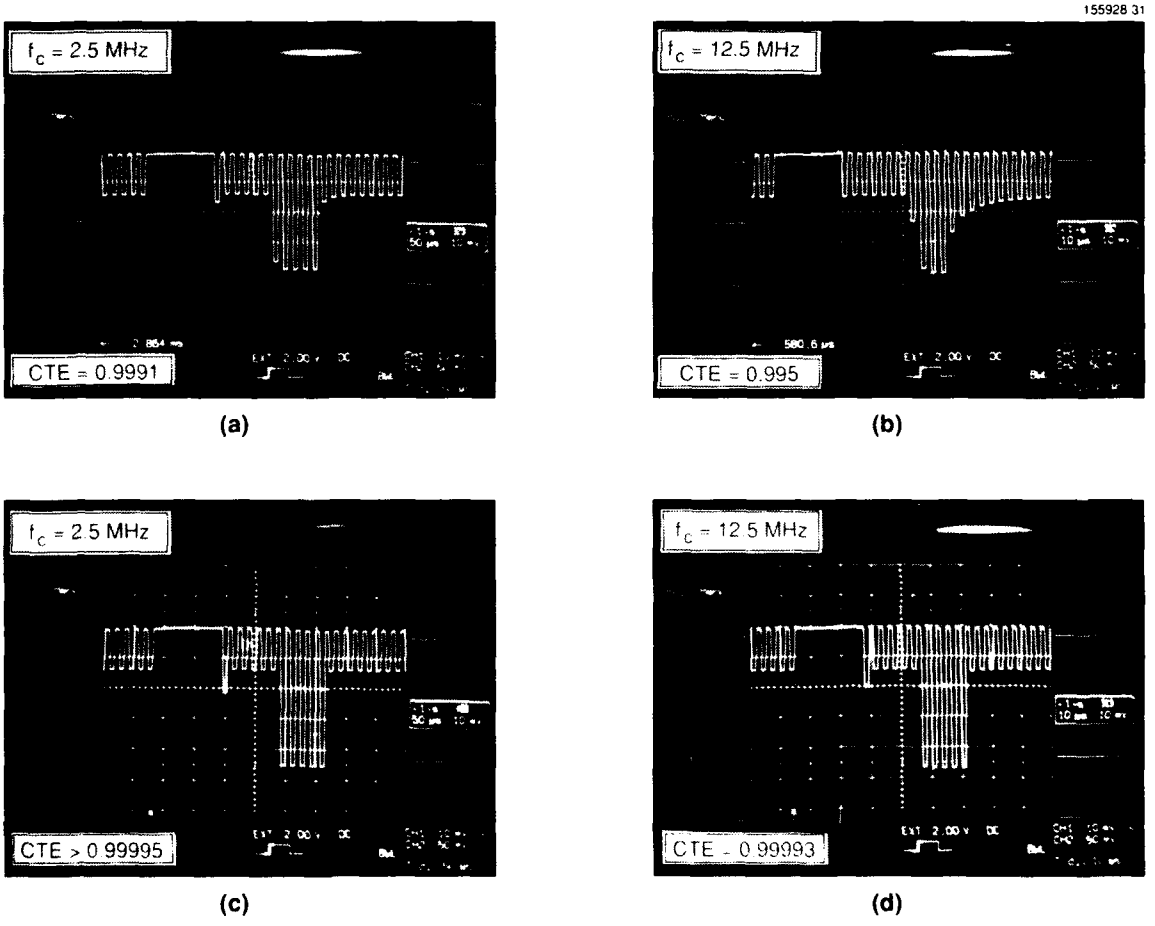

Figure 6-3. Output from long-gate (L = 26 μm) CCDs, when the input is one pulse, 5 clock periods wide, for the following devices: (a) uniform, f_c = 2.5 MHz, (b) uniform, f_c = 12.5 MHz, (c) step-doped, f_c = 2.5 MHz, (d) step-doped, f_c = 12.5 MHz.

Short-channel CCDs with the built-in drift fields were tested up to the 325-MHz limit of the existing clock drivers. At this rate, the transfer loss is barely measurable (CTE = 0.99995). In the uniform short-channel CCDs, the transfer loss is too small to measure for $f_c < 240$ MHz (CTE > 0.99996) but increases very rapidly for higher clocking rates. The transfer time corresponding to $f_{c(max)} = 240$ MHz is 1.1 ns. For the step-doped short-channel CCDs, given the limitations of the existing clock drivers, we can determine only that $f_{c(max)} \geq 325$ MHz and the transfer time is ≤ 0.54 ns. Figure 6-4 shows the outputs for uniform and step-doped short-channel CCDs at 240 and 325 MHz. The experimentally measured improvement in the transfer time is consistent with our expectations.

The step implant is a simple processing step that can dramatically improve the performance of CCDs. In addition to enhancing the electron drift, the built-in fields overcome imperfections and bulk trapping in long-channel devices, resulting in improved performance even at very low clocking rates. Step doping

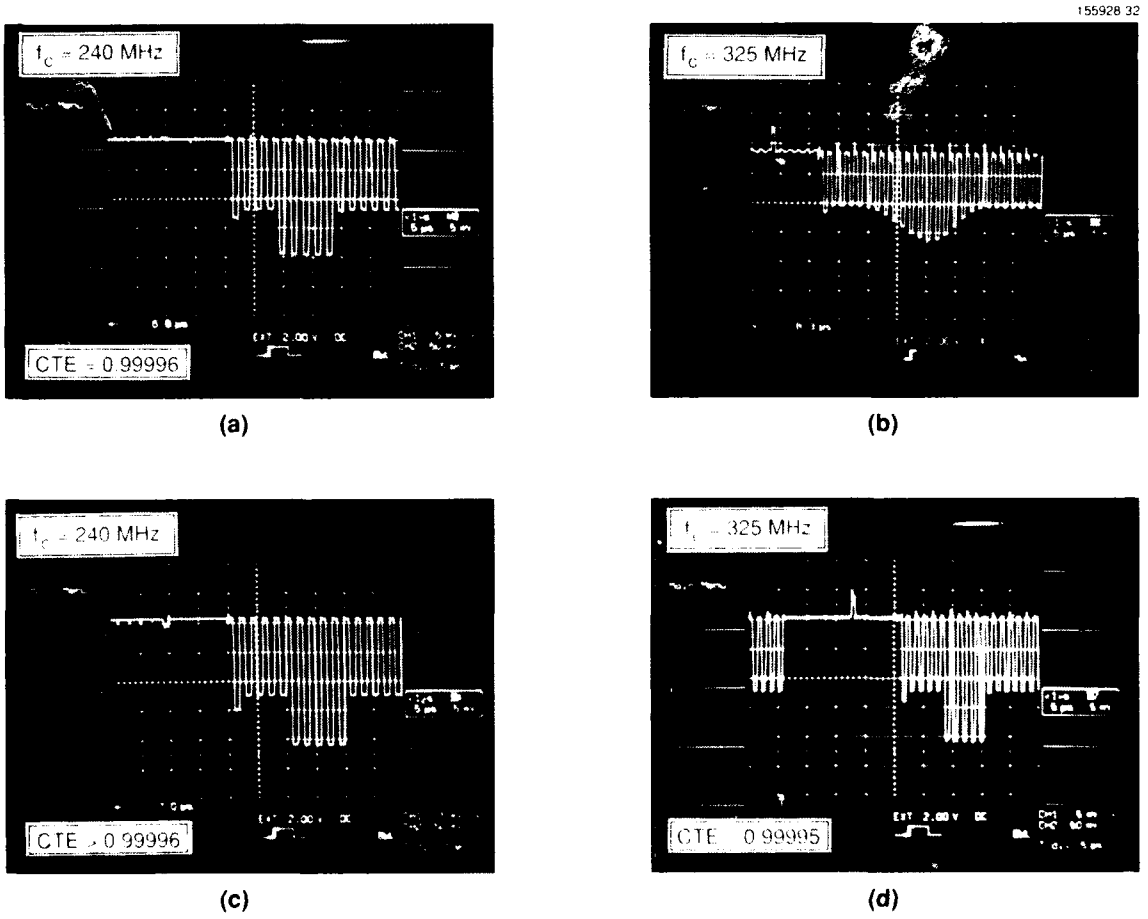

Figure 6-4. Output from short-gate ($L_c = 7$ μm) CCDs, when the input is one pulse, 5 clock periods wide, for the following devices. (a) uniform, $f_c = 240$ MHz. (b) uniform, $f_c = 325$ MHz. (c) step-doped, $f_c = 240$ MHz. (d) step-doped, $f_c = 325$ MHz.

provides the designer with an important additional degree of freedom. With it, CCD clock rates can be increased without reducing gate lengths. Alternatively, step doping makes it possible to increase gate length and/or increase the number of stages while retaining adequate CTE for a given clock rate.

A.L. Lattes
S.C. Munroe
M.M. Seaver

6.2 ACQUISITION/PREPROCESSING SUBSYSTEM FOR A Nd-LASER RADAR SYSTEM

To test an a Nd-laser radar system, an acquisition/preprocessing subsystem was built whose capabilities include a 200-MHz bandwidth (~ 1-m range resolution), a 6-bit amplitude resolution, a 150-m range swath (1-μs return window), and a return rate of up to 80 pulses/s. Intended for integration within the Lincoln Laboratory Firepond Facility for radar experimentation, this subsystem will trigger a compact solid state Nd laser to transmit through the telescope optics at the facility and will acquire and preprocess the subsequent radar returns. To accelerate the configuration of the subsystem and to provide sufficient capability for reconfigurations as requirements evolve, only commercially available test-and-measurement equipment was utilized.

A simplified block diagram of the Nd-laser radar system is shown in Figure 6-5. To ensure synchronization to the transmit/receive chopper a timing signal from the Firepond hardware is provided. This signal is used to generate laser-diode-pump and Q-switch-trigger signals to the Nd laser. The output of the laser is frequency doubled (into the green region) and transmitted through the chopper and telescope optics. A fraction of the transmitted 5- to 30-ns light pulse energy is detected, sampled and stored as a reference to indicate the exact time of the transmitted pulse. The returned pulses are detected using a four-quadrant photomultiplier tube, and each quadrant is fed to one of four data-acquisition channels. The trigger to begin acquisition of returned pulses is supplied by a programmable digital-delay pulse generator. For the first experiments, the target will be tracked and this delay supplied by a CO_2 laser tracking system operating at Firepond concurrently with the Nd-laser radar system. In later experiments, acquisition and tracking algorithms will be incorporated within the Nd-laser radar system.

As shown in Figure 6-5, the trigger and timing circuitry of the Nd-laser radar system receives global timing information from the Firepond hardware. These lines provide transmit triggers and range-word handover. Within the system, the transmit triggers are fed to programmable digital-delay pulse generators to provide the multiple, properly delayed triggers required by the transmit and receive portions of the system. The time delay in these generators is accurate to within a small fraction of a nanosecond. The system is capable of providing the Nd-laser transmitter a burst of up to four triggers; these are appropriately spaced within a 4-ms transmit window, with each 100-ms acquisition cycle consisting of two such windows. To achieve this, each Firepond master trigger produces a burst of pulses by summing the outputs of four simultaneously triggered pulse generators. The time delay between the pulses within the burst is programmed by a computer.

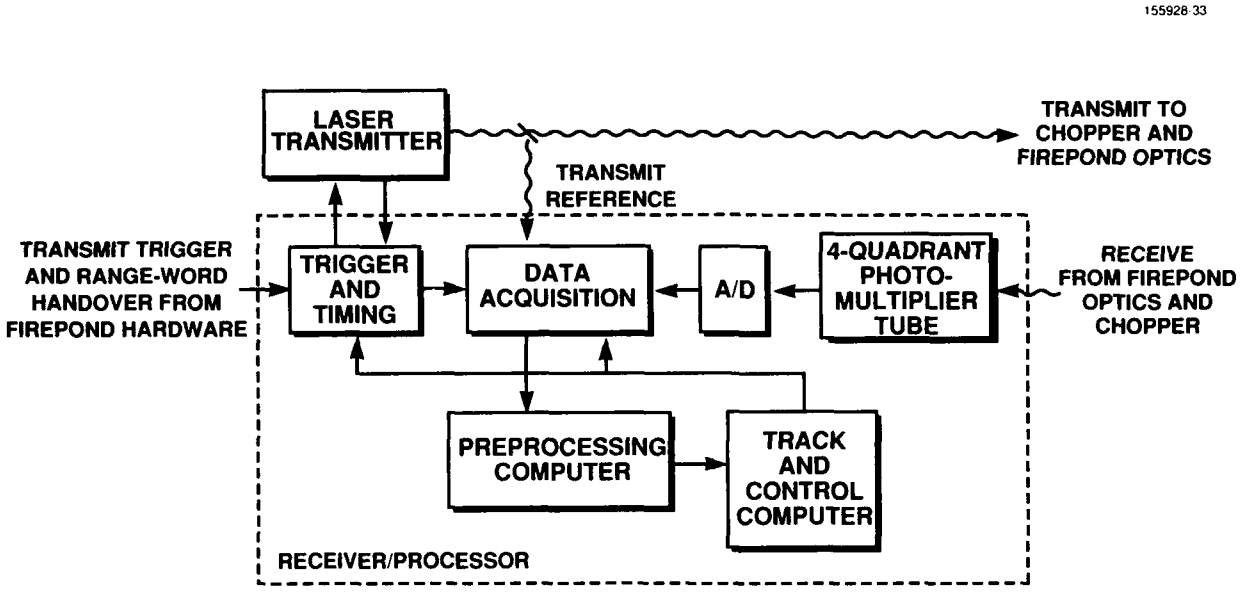

Figure 6-5. Block diagram of the Nd-laser radar system. The acquisition/preprocessing features of the system include a 200-MHz bandwidth (~ 1-m range resolution), a 6-bit amplitude resolution, a 150-m range swath (1-μs window), and a pulse-return rate of up to 80 pulses/s.

The data-acquisition units are dual-channel digital transient-data oscilloscopes capable of 400-MHz sampling rates. Three of these units are used for the required five channels of data acquisition, consisting of one channel for the transmitted reference signal and four channels for the returned signals. At a 400-MHz rate, 400 samples are simultaneously taken of each of the return signals over a 1-μs window. The acquisition oscilloscopes are programmed to acquire from 2 to 8 pulses during each acquisition cycle of 100 ms. Following each cycle, the sampled data is transferred from oscilloscope memory through a general-purpose interface bus (GPIB) into memory within the preprocessing computers. Three such computers are required, one for each oscilloscope. Each of the two computers servicing the receive oscilloscopes must transfer the data from two receive channels and rearm the units for subsequent acquisitions. The third computer, used for servicing the transmit oscilloscope, needs to transfer only one significantly smaller packet of data during each 100-ms cycle time, so it is further utilized to consolidate the data for subsequent processing. The required data throughput was near the limits of the GPIB employed. The computers were loaded with the maximum possible random-access memory to provide sufficient high-speed memory to acquire 4 to 5 min of data without the need to transfer data to a slower storage medium. The overall system provides real-time display of target position within the acquisition window as well as real-time gain control and range-word storage for post-mission trajectory display.

D.R. Arsenault
J.H. Holtham
A.P. Denneno

REPORT DOCUMENTATION PAGE

Form Approved
OMB No. 0704-0188

1. AGENCY USE ONLY *(Leave blank)*	2. REPORT DATE	3. REPORT TYPE AND DATES COVERED
	15 May 1990	Quarterly Technical Report, 1 February — 30 April 1990

4. TITLE AND SUBTITLE

Solid State Research

5. FUNDING NUMBERS

C — F19628-90-C-0002
PE — 63250F
PR — 221

6. AUTHOR(S)

Alan L. McWhorter

7. PERFORMING ORGANIZATION NAME(S) AND ADDRESS(ES)

Lincoln Laboratory, MIT
P.O. Box 73
Lexington, MA 02173-9108

8. PERFORMING ORGANIZATION REPORT NUMBER

1990:2

9. SPONSORING/MONITORING AGENCY NAME(S) AND ADDRESS(ES)

Air Force Systems Command, USAF
Andrews AFB
Washington, DC 20334-5000

10. SPONSORING/MONITORING AGENCY REPORT NUMBER

ESD-TR-90-087

11. SUPPLEMENTARY NOTES

None

12a. DISTRIBUTION/AVAILABILITY STATEMENT

Approved for public release; distribution is unlimited.

12b. DISTRIBUTION CODE

13. ABSTRACT *(Maximum 200 words)*

This report covers in detail the research work of the Solid State Division at Lincoln Laboratory for the period 1 February through 30 April 1990. The topics covered are Electrooptical Devices, Quantum Electronics, Materials Research, Submicrometer Technology, Microelectronics, and Analog Device Technology. Funding is provided primarily by the Air Force, with additional support provided by the Army, DARPA, Navy, SDIO, NASA, and DOE.

14. SUBJECT TERMS

electrooptical devices	microelectronics	nonlinear optics	mass memory
quantum electronics	analog device technology	crystal growth	quantum-well devices
materials research	lasers	Schottky barriers	charge-coupled devices
submicrometer technology	optical modulators	excimer lithography	

15. NUMBER OF PAGES
86

16. PRICE CODE

17. SECURITY CLASSIFICATION OF REPORT	18. SECURITY CLASSIFICATION OF THIS PAGE	19. SECURITY CLASSIFICATION OF ABSTRACT	20. LIMITATION OF ABSTRACT
Unclassified	Unclassified	SAR	